BRD4 orchestrates genome folding to promote neural crest differentiation

Ricardo Linares-Saldana[1,2,3,‡], **Wonho Kim**[1,2,3,‡], **Nikhita A. Bolar**[1,2,3,‡], **Haoyue Zhang**[4,5], **Bailey A. Koch-Bojalad**[1,2,3], **Sora Yoon**[1,3,6,7], **Parisha P. Shah**[1,2,3], **Ashley Karnay**[1,2,3], **Daniel S. Park**[1,3,6], **Jennifer M. Luppino**[1,3,6], **Son C. Nguyen**[1,3,6], **Arun Padmanabhan**[8,9], **Cheryl L. Smith**[1,2,3], **Andrey Poleshko**[1,2,3], **Qiaohong Wang**[1,2,3], **Li Li**[1,2,3], **Deepak Srivastava**[8,10], **Golnaz Vahedi**[1,3,6,7,11], **Gwang Hyeon Eom**[1,2,3,12], **Gerd A. Blobel**[1,3,5], **Eric F. Joyce**[1,3,6], **Rajan Jain**[1,2,3,*]

[1]Perelman School of Medicine, University of Pennsylvania, Philadelphia, PA, USA

[2]Department of Cell and Developmental Biology, Department of Medicine, Institute of Regenerative Medicine, Penn Cardiovascular Institute, University of Pennsylvania, Philadelphia, PA, USA

[3]Penn Epigenetics Institute, University of Pennsylvania, Philadelphia, PA, USA

[4]The Shenzhen Bay Laboratory, Shenzhen, China

[5]Division of Hematology, The Children's Hospital of Philadelphia, Philadelphia, PA, USA

[6]Department of Genetics, University of Pennsylvania, Philadelphia, PA, USA

[7]Institute for Immunology, Epigenetics Institute, Institute for Diabetes, Obesity and Metabolism, University of Pennsylvania, Philadelphia, PA, USA

[8]Gladstone Institute of Cardiovascular Disease, San Francisco, CA, USA

[9]Division of Cardiology, Department of Medicine, University of California, San Francisco, CA, USA

[10]Roddenberry Stem Cell Center at the Gladstone Institutes, Departments of Pediatrics and Biochemistry & Biophysics, University of California San Francisco, San Francisco, CA, USA

[11]Abramson Family Cancer Center, University of Pennsylvania, Philadelphia, PA, USA

[12]Department of Pharmacology, Chonnam National University Medical School, Hwasun, Republic of Korea

---

[*]Address correspondence to: Rajan Jain, Perelman School of Medicine, 3400 Civic Center Blvd, Philadelphia, PA 19104, jainr@pennmedicine.upenn.edu.
[‡]These authors contributed equally to this work.

Abstract

Higher-order chromatin structure regulates gene expression, and mutations in proteins mediating genome folding underlie developmental disorders known as cohesinopathies. However, the relationship between three-dimensional genome organization and embryonic development remains unclear. Here, we define a role for Bromodomain-containing protein 4 (BRD4) in genome folding and leverage it to understand the importance of genome folding in neural crest progenitor differentiation. *Brd4* deletion in neural crest results in cohesinopathy-like phenotypes. BRD4 interacts with NIPBL, a cohesin agonist, and BRD4-depletion or loss of the BRD4-NIPBL interaction reduces NIPBL occupancy, suggesting BRD4 stabilizes NIPBL on chromatin. Chromatin interaction mapping and imaging experiments demonstrate that BRD4-depletion results in compromised genome folding and loop extrusion. Finally, mutation of individual BRD4 amino acids that mediate an interaction with NIPBL impedes neural crest differentiation into smooth muscle. Remarkably, loss of WAPL, a cohesin antagonist, rescues attenuated smooth muscle differentiation resultant of BRD4 loss. Collectively, our data reveal that BRD4 choreographs genome folding and illustrate the relevance of balancing cohesin activity on progenitor differentiation.

Introduction

Organogenesis requires coordinated progressive lineage restriction and differentiation of progenitor cells into specific cell types. The neural crest is a population of cells critical for the development of several ectodermal and mesodermal tissues[1]. These cells delaminate from the neural tube and differentiate into a variety of specialized cells and tissues, including melanocytes, craniofacial bones and cartilage, and enteric nerves in the intestinal tract[2]. A subset of neural crest cells directs septation of the cardiac outflow tract and contributes to smooth muscle surrounding the aorta and pulmonary artery[3]. Impaired neural crest differentiation is implicated in the etiology of neurocristopathies, which often result in outflow tract morphogenesis defects, cleft palate and craniofacial abnormalities[4]. Thus, determining the gene regulatory networks and molecular determinants underlying neural crest differentiation will inform our understanding of neurocristopathies and related diseases.

Emerging evidence links gene regulation to higher-order chromatin structure[5], suggesting a role for genome organization in development and tissue homeostasis. Recent studies have identified self-interacting areas of the genome that are important for gene expression. These domains are often composed of a nested series of discrete, and likely dynamic, chromatin interactions[6]. The physiologic relevance of genome folding is of intense interest, as are the roles of specific genome organization factors in disease. The multisubunit cohesin ring complex has been shown to be a critical regulator of genome folding[7]; loss of core cohesin complex subunits results in a loss of loop domains in population-based genomic studies[8,9]. Of particular interest, human mutations in the cohesin complex have been linked to leukemias and a group of diseases collectively termed cohesinopathies, which include Cornelia de Lange Syndrome (CdLS) and related syndromes[10,11]. Multiple organ systems are often affected and syndromes share overlapping phenotypes. CdLS patients present with craniofacial abnormalities, including cleft lip and dental defects, intellectual disability, and

delayed ossification of various bones. Approximately one-third of patients also present with congenital heart disease[12]. Despite the rich human genetic data underlying cohesinopathies, the mechanistic relationship between cohesin function and pathogenesis remains unclear.

CdLS is frequently associated with heterozygous loss-of-function mutations in *NIPBL*, which encodes a positive effector of cohesin that facilitates loading of the cohesin onto chromatin[10,13,14]. *In vitro* reconstitution assays show that NIPBL enables cohesin to extrude loops of chromatin[15,16]. Accordingly, genetic loss of *Nipbl* in mice results in a loss of topologically associating domains (TADs) and chromatin loops[17] and recapitulates phenotypes observed in cohesinopathies and CdLS[18]. Interestingly, patients with mutations in *BRD4* (Bromodomain-containing protein 4) can present with cohesinopathy features, particularly CdLS[19,20]. BRD4 is a member of the Bromodomain and Extraterminal domain (BET) protein family, characterized by tandem bromodomains that recognize acetylated lysine residues on histone and non-histone proteins[21]. BRD4 is one of only a few non-core cohesin proteins that have been found to be mutated in CdLS. Though BRD4 and NIPBL interact[20,22], the functional nature of this relationship remains elusive, particularly if and how BRD4 modulates NIPBL and/or cohesin function and how this interaction directs tissue development.

BRD4 has a well-established role in recruiting transcriptional machinery upon binding to acetylated histones to mediate transcriptional pause release[23]. Here, we reveal a role for BRD4 in mediating genome folding by stabilizing NIPBL on chromatin and thereby promoting neural crest progenitor differentiation. Loss of *Brd4* in neural crest cells *in vivo* results in phenotypes similar to cohesinopathies. Mechanistically, acute degradation of BRD4 protein results in diminished NIPBL chromatin occupancy and loss of normal genome folding, as assessed by high-throughput chromosome conformation capture (Hi-C). Oligopaints-based DNA fluorescence *in situ* hybridization (Oligopaints FISH[24]) studies in cells acutely depleted of BRD4 or expressing BRD4 point mutants unable to bind NIPBL further demonstrate the importance of the BRD4-NIPBL complex in proper genome folding. Moreover, the role of BRD4 in genome folding is separate from its role in promoting transcription. Finally, a combination of *in vivo* and *in vitro* experiments demonstrate that BRD4 is required for neural crest differentiation into smooth muscle via an interaction with NIPBL. Remarkably, smooth muscle differentiation defects resulting from loss of BRD4 can be rescued by depletion of WAPL, a negative regulator of cohesin[25–28], demonstrating the functional relevance of BRD4 regulation of cohesin function. Taken together, by deciphering BRD4's role in maintaining genome topology, we establish the physiologic relevance of balancing cohesin activity on cell fate determination.

Results

Brd4 *loss in neural crest resembles cohesinopathies*

We crossed mice harboring loxP sites flanking exon 3 (canonical ATG) of *Brd4*[29,30] with mice expressing Cre recombinase under the control of a *Wnt1* enhancer active in pre-migratory neural crest cells and in neural crest immediately following their delamination from the neural tube[31]. We confirmed efficient, tissue-specific deletion of *Brd4* (Fig. 1a). We were unable to recover any mutant (*Brd4*[f/f], *Wnt1*Cre+) embryos after postnatal day

1, indicating that BRD4 is essential in neural crest cells and required for development and mouse viability (Supplementary Table 1). BRD4-mutant late gestation embryos exhibited skeletal dysplasia coupled with several highly penetrant craniofacial defects including loss of forehead contouring, microcephaly, micrognathia, and loss of neural-crest-derived middle ear bones (Fig. 1b; Supplementary Table 1). In addition, all mutants demonstrated a cleft palate, which likely accounts for the observed perinatal lethality (Fig. 1c). Abnormal tooth formation was also observed (Fig. 1c, right). Despite loss of BRD4, neural crest derivatives were still able to populate the developing craniofacial structures as evidenced by lineage-tracing studies (Fig. 1d and Extended Data Fig. 1a).

Consistent with the role for neural crest in outflow tract development, the majority of late gestation $Brd4^{f/f}$, $Wnt1$Cre+ embryos analyzed showed ventricular septal defects compared to zero littermate controls (Fig. 1e; Supplementary Table 1). Approximately one-half of late gestation embryos demonstrated more complex heart defects, including persistent truncus arteriosus, double outlet right ventricle (DORV) and abnormal aortic arch artery patterning, consistent with a defect in cardiac neural crest[3] (Fig. 1e, Extended Data Fig. 1b; Supplementary Table 1). Given the craniofacial and cardiac abnormalities observed, we assessed proliferation in neural-crest-derived mesenchyme. We found a significant reduction in the percentage of phospho-histone H3-positive cells at embryonic day 11.5 (E11.5) $Brd4^{f/f}$, $Wnt1$Cre+, $R26^{mt-mg/+}$ embryos compared to $Brd4^{f/+}$, $Wnt1$Cre+, $R26^{mt-mg/+}$ embryos consistent with the known role of BRD4 in cell proliferation (Extended Data Fig. 1c).

Collectively, these data establish that neural-crest-specific $Brd4$ deletion results in a range of craniofacial, skeletal, and cardiac defects coupled with perinatal lethality. Loss of $Nipbl$ or its related factor $Mau2$ during embryogenesis results in a similar phenotype to those observed in the $Brd4^{f/f}$, $Wnt1$Cre+ embryos[18,32] (Supplementary Table 1). Heterozygous global loss of $Nipbl$, including on a sensitized genetic background, results in ventricular septal and outflow tract defects[32]. Notably, expression of $Nipbl$ and $Smc1a$, a subunit of the cohesin ring, were not affected by loss of $Brd4$ in the neural crest-derived secondary palate of $Brd4^{f/f}$, $Wnt1$Cre+ embryos (Extended Data Fig. 1d). Given these phenotypes within the context of recent BRD4-CdLS human genetic studies mentioned above, we examined the interaction between BRD4 and NIPBL and tested the hypothesis that loss of BRD4 results in aberrant NIPBL and/or cohesin function.

A hydrophobic cleft in BRD4 ET domain mediates NIPBL interaction

Reciprocal co-immunoprecipitation assays confirmed the known interaction between BRD4 and NIPBL[20,22] in murine embryonic stem cells (mESCs) and HEK293T cells (Fig. 2a). These results are consistent with previous studies in a cell-free system[22], and systematic analysis using human BRD4 (hBRD4) fragments (Fig. 2b) indicated that the ET domain was sufficient to interact with NIPBL (Fig. 2c). Relevant to our mouse genetic studies, we immunoprecipitated endogenous BRD4 from neural crest progenitor cells[33] and observed co-precipitation of endogenous NIPBL (Extended Data Fig. 1e). Addition of a small-molecule degrader of BET proteins (MZ3[34]) resulted in a reduction in the amount of BRD4 detected. Specificity of the interaction was further validated by reduction of the

immunoprecipitation window to 30 minutes (Extended Data Fig. 1f). RAD21 and SMC1a, both cohesin ring subunits, and MAU2, which heterodimerizes with NIPBL[35], also co-immunoprecipitated with BRD4, though the band intensity of each protein was relatively weaker compared to NIPBL (Extended Data Fig. 1g,h).

Nuclear magnetic resonance spectroscopy studies have revealed the structure of the BRD4 ET domain[36] (Fig. 2d). To identify residues critical for NIPBL interaction, we generated a series of point mutations within a hydrophobic pocket of the ET domain that has been shown to be critical to interact with proteins such as NSD3[36,37]. We expressed either FLAG-tagged wildtype hBRD4 or full-length hBRD4 harboring various mutations in the ET domain. Deletion of the ET domain (dET) or introduction of point mutations (L630W, V634W, I654Q, F656W and E653R/D655R) into the hydrophobic pocket resulted in a reduction or loss of interaction with NIPBL (Fig. 2e). An ET domain point mutation (R669H) outside of the hydrophobic pocket did not disrupt NIPBL binding (Fig. 2e). We found a similar trend with MAU2 (Extended Data Fig. 1i), consistent with a report indicating MAU2 chromatin binding depends on NIPBL[35]. In addition, BRD4-L630W, -I654Q, -F656W and -E653R/D655R also eliminated the known interaction with NSD3[37], while BRD4-V634W did not perturb the NSD3 interaction to the same degree. All BRD4 mutants retained the ability to interact with histone H4 acetylated on lysines 5, 8, 12, and 16, known to be strongly bound by BRD4[38], suggesting that loss of NIPBL interaction was not a result of abrogated chromatin binding. Studies have identified peptide sequences from BRD4 interacting proteins that may bind the ET domain (Extended Data Fig. 1j)[36,39]. Alignment of these sequences revealed a consensus motif of Φ-K/R-Φ-X-K/R (Φ: hydrophobic amino acid; X: any amino acid). A sequence in the N-terminus of NIPBL aligns with the consensus sequence, and it is predicted to have an α-helical structure similar to the BRD4-interacting domain in JMJD6 (Extended Data Fig. 1j)[40]. Collectively, these biochemical experiments identify the specific residues within the hydrophobic cleft of the BRD4 ET domain that mediate this interaction.

BRD4 stabilizes NIPBL binding on chromatin

Consistent with our interaction studies, previous reports have shown that BRD4 and NIPBL both co-occupy regulatory elements[41,42]. Analysis of publicly available mESC ChIP-seq datasets (GSM937540-BRD4, GSM560350-NIPBL) revealed that ~66% of peaks were co-occupied by BRD4 and NIPBL (21,327 shared sites, 34,794 total BRD4 sites, 34,942 total NIPBL sites; Extended Data Fig. 2a; Supplementary Table 2). Therefore, we sought to assess whether BRD4 is necessary for NIPBL occupancy on chromatin. We generated mESCs in which a degron epitope tag (dTAG) was introduced immediately after the conserved endogenous start codon of *Brd4* on both alleles[43] (hereafter referred to as dTAG-BRD4 mESCs, Fig. 3a, Extended Data Fig. 2b,c). The dTAG insertion was confirmed by PCR amplification and Sanger sequencing (Extended Data Fig. 2b). Introduction of the epitope did not substantially alter the levels of chromatin-bound BRD4 in the dTAG-BRD4 mESCs compared to the parental mESC line (Extended Data Fig. 2c). Addition of a dTAG ligand (dTAG-13), renders the tagged BRD4 protein sensitive to proteasomal degradation, enabling depletion of BRD4 in an acute and efficient manner (dTAG-13-treated dTAG-BRD4 mESCs, hereafter "degron"). All experiments, unless otherwise indicated, used naïve

mESCs, in which the short isoform of BRD4 is not expressed[44]. After optimizing isolation of chromatin fractionations (Extended Data Fig. 2d), we confirmed that chromatin-bound BRD4 was efficiently degraded in both a dTAG-13 dose- and time-dependent manner (Fig. 3b,c). In addition, OCT4 (also known as POU5F1) was expressed in dTAG-BRD4 mESCs treated with either DMSO or dTAG-13 for 4.5 hours (Extended Data Fig. 2e). Importantly, acute degradation of BRD4 for 4.5 hours did not result in substantial changes in proliferation compared to DMSO-treated dTAG-BRD4 mESCs (Extended Data Fig. 2f). Taking this into account, and the estimated mESC doubling time of ~8–10 hours[45], we proceeded with experiments using cells treated with dTAG-13 or DMSO for 4.5 hours (unless otherwise noted).

We employed Cleavage Under Target and Release Under Nuclease (CUT&RUN) to map BRD4 and NIPBL occupancy in dTAG-BRD4 mESCs treated with DMSO or degron (n = 3 replicates; Supplementary Table 2). After confirming reproducibility, datasets were merged, scaled and read-depth normalized for intra-condition comparison as previously described[46] (see Methods; Supplementary Table 2). We detected enrichment of NIPBL and BRD4 at previously defined BRD4 and NIPBL peaks, as well as substantial co-occupancy between the factors in DMSO-treated cells (Fig. 3d,e, and Extended Data Fig. 3a). In addition, BRD4 occupancy was dramatically reduced in degron samples (Fig. 3d,e, Extended Data Fig. 3a). Strikingly, NIPBL occupancy was also decreased in the degron samples (Fig. 3d,e and Extended Data Fig. 3a,b). Further, we also observed a moderate reduction in chromatin-bound NIPBL in cells treated with dTAG-13, dTAG^v-1, an alternative dTAG ligand[47], or MZ3 (Extended Data Fig. 3c). Similarly, we performed CUT&RUN to assess acetylation of lysine 27 on histone H3 (H3K27ac), a post-translational modification enriched in active regulatory regions[48]. We confirmed enrichment of H3K27ac in DMSO cells at previously annotated H3K27ac peaks (GSM2588454) and observed no clear changes in the H3K27ac profile in the degron samples (Fig. 3d,e and Extended Data Fig. 3a), indicating that reduced NIPBL occupancy and other phenotypes described below that are resultant of BRD4-depletion cannot be attributed to H3K27ac loss.

We next assessed if the BRD4-NIPBL interaction was necessary to maintain NIPBL on chromatin by leveraging the aforementioned NIPBL binding-defective BRD4 mutants (BRD4-dET, -L630W, and -V634W). First, we established conditions in which the expression levels of exogenous wildtype or BRD4-mutants was comparable across conditions upon degradation of endogenous BRD4 (Extended Data Fig. 3d). Next, we performed ChIP-qPCR at two loci with substantial BRD4 and NIPBL occupancy (Fig. 3e,f). Loss of endogenous BRD4 resulted in a significant reduction in NIPBL occupancy, but unchanged H3K27ac enrichment (Fig. 3f and Extended Data Fig. 3e). Importantly, exogenous expression of full-length BRD4 normalized NIPBL occupancy, whereas expression of BRD4 ET deletion or point mutants reduced NIPBL occupancy at both loci (Fig. 3f). BRD4 enrichment was comparable at these sites in the cultures expressing exogenous BRD4 (Extended Data Fig. 3f). Together, these data support a model in which BRD4 stabilizes NIPBL on chromatin, likely through an interaction in the ET domain.

BRD4 maintains genome folding by interacting with NIPBL

Loss of *Nipbl* in post-natal hepatocytes results in a loss of chromatin loops and a weakening of TADs[17]. Given the decrease in NIPBL occupancy upon acute BRD4 depletion, we assessed the impact of acute BRD4 loss on higher-order chromatin organization. We performed *in situ* Hi-C[49] in two biological replicates of DMSO and degron dTAG-BRD4 mESCs, each (Fig. 4a). After confirming the data quality and reproducibility, replicate reads were pooled, mapped, filtered for valid interactions, binned, and normalized based on the HiC-Pro pipeline to generate normalized and balanced contact maps[50] (see Methods; Supplementary Table 2). In total, we sequenced ~1 billion paired-end reads per condition, which resulted in 291,168,696 and 245,410,300 contacts from the DMSO and degron-treated cells, respectively, post-filtering.

Visual inspection of interaction matrices suggested a general weakening of interactions upon acute BRD4 loss (Fig. 4a). To quantitatively assess changes genome-wide, we identified focal areas of high interaction frequency between two distal regions of the genome, often referred to as chromatin loops[7,51,52]. We benchmarked loop calling algorithms against a high-resolution mESC contact matrix[53] and arrived at an optimal set of parameters using c-Loops[54] to identify chromatin loops that substantially overlapped with previously published SMC1a-anchored loops[55] (Extended Data Fig. 4a). Approximately half of the loops in DMSO-treated cells were associated with a BRD4 peak at one or both anchors (n = 3,860/7,517). Moreover, strength of loops identified in DMSO cells significantly decreased upon BRD4 depletion (Fig. 4b,c; Supplementary Table 3).

We then stratified loops as either lost (sensitive to BRD4 loss and hence identified in DMSO but not in degron, hereafter 'BRD4-sensitive') or retained (resistant to BRD4 loss and identified in both conditions, hereafter 'BRD4-resistant'). The majority of loops in the DMSO dataset were BRD4-sensitive (n = 5,298/7,517 loops), and therefore not identified in the degron condition. There was a clear reduction in the contact frequency (normalized mean counts/bin) for BRD4-sensitive loops upon BRD4 depletion (Fig. 4b) and aggregate analysis of this loop subset confirmed sensitivity to BRD4 depletion (Fig. 4c). Approximately 30% of loops identified in DMSO were BRD4-resistant (Fig. 4b,c, n = 2,219/7,517). While BRD4-resistant loops lost strength upon BRD4 depletion, the change in strength was expectedly not as dramatic as BRD4-sensitive loops. Our analyses also revealed newly formed loops in the degron condition, but there was a minimal increase in counts in the degron condition, especially in comparison to the change observed in BRD4-sensitive loops (Extended Data Fig. 4b). Therefore, we focused subsequent analyses on BRD4-sensitive and BRD4-resistant regions/loops.

BRD4-sensitive loop anchors were enriched for BRD4 and NIPBL occupancy compared to BRD4-resistant loop anchors (Fig. 4d and Extended Data Fig. 4c). Furthermore, the majority of BRD4-resistant loops were enriched for features consistent with structural loops, previously defined as loops containing CTCF and cohesin peaks at both anchors and H3K27ac peaks at no more than one anchor[56] (Extended Data Fig. 4d). In a reciprocal approach, we calculated genome-wide insulation scores in 40-kb bins in DMSO- and degron-treated cells and calculated the change in interaction frequency around BRD4 and NIPBL peaks. The interaction frequency inversely correlates with the insulation score[57],

and interaction frequency decreased around regions identified as BRD4 or NIPBL peaks as opposed to regions bound by other architectural proteins (Extended Data Fig. 4e). Visual inspection of the interaction matrices and the loop analyses suggests that some regions are more vulnerable to decreases in interaction frequency than others upon BRD4 degradation, and the amount of BRD4 and NIPBL occupancy broadly correlated (Extended Data Fig. 3a). Therefore, we plotted change in interaction frequency based on stratification of BRD4 and NIPBL peak strength in DMSO cells. Areas with the highest BRD4 peak strength showed the greatest decrease in interaction frequency, and these regions also displayed the greatest NIPBL occupancy. In contrast, areas with weaker BRD4 peaks demonstrated smaller changes in interaction frequency and lower NIPBL occupancy (Fig. 4e). A similar trend was also observed for changes in interaction frequency relative to NIPBL peak strength (Extended Data Fig. 4f).

In addition to changes in chromatin loops, visual inspection of the interaction matrix suggested a weakening of TADs[51] (Fig. 4a). We identified ~4,800 TADs in DMSO-treated dTAG-BRD4 mESCs, similar to previous reports (Jaccard index = 0.82 compared to Dixon et al., 2012; Extended Data Fig. 4g; Supplementary Table 3)[53]. TADs showed reduced interaction frequency/weakening upon BRD4 depletion (Fig. 4f,g, top row). To extend this observation, we determined the percentage change in the mean interaction frequency for each TAD defined in the DMSO dataset upon BRD4 depletion (Fig. 4h). This assessment confirmed that a subset of TADs was uniquely sensitive to BRD4 depletion (Fig. 4f,g; top and bottom decile of TADs changing, respectively), and similar to the loop analysis, BRD4-sensitive TADs were also enriched in BRD4/NIPBL peaks (Fig. 4h). Moreover, unlike intra-TAD interaction frequency, we found insulation at boundaries between TADs did not vary substantially (DMSO and degron insulation score Spearman correlation = 0.97, Extended Data Fig. 4h). Finally, we did not detect substantial changes in compartmentalization (Extended Data Fig. 5). Taken together, these data indicate that organization of a subset of loops and TADs are dependent on BRD4.

To validate the Hi-C findings, we designed Oligopaints FISH probes to three genomic regions that demonstrated a reduction in NIPBL occupancy and interaction frequency upon BRD4-depletion (Fig. 5a and Extended Data Fig. 6a,d,e; Supplementary Table 4). Our group has shown that TAD changes can be visualized using such an approach[58]. NIPBL depletion resulted in a significant increase in center-to-center distance between FISH signals (Fig. 5a,b and Extended Data Fig. 6b), consistent with published reports[17,25,58]. BRD4-depletion also resulted in a significant increase in center-to-center distance between signals with minor changes in individual probe geometry (Fig. 5a,c and Extended Data Fig. 6c; representative replicate shown). We also observed increased center-to-center FISH probe distances at a different locus with the aforementioned characteristics (Extended Data Fig. 6d). A third locus with less BRD4 and NIPBL occupancy in DMSO samples than the other two loci (and at which we observed a smaller change in interaction frequency in our Hi-C studies upon BRD4 depletion), yielded a significant, but relatively attenuated increase in center-to-center distances (Extended Data Fig. 6e). Thus, Oligopaints FISH probes targeted to three loci validated our Hi-C results indicating a critical role for BRD4 in maintaining TAD interactions.

In order to further examine the role of BRD4-NIPBL interaction in mediating genome folding, we introduced GFP-fused NIPBL-binding-defective hBRD4 constructs (BRD4-dET, -L630W and -V634W) into dTAG-BRD4 mESCs (in a manner identical to Fig. 3f). We confirmed GFP expression in the majority of cells (Extended Data Fig. 6f). Subsequently, we depleted endogenous BRD4 for 4.5 hours and performed FISH for the regions indicated in Fig. 5a (Fig. 5c). Wildtype GFP-hBRD4 maintained normal probe-to-probe distance; however, each NIPBL-binding defective mutant increased center-to-center distances compared to wildtype GFP-hBRD4 or control cells. The enrichment of chromatin bound GFP-hBRD4 was comparable at two different sites in the regions painted by FISH probes (Extended Data Fig. 6g). Individual probe geometry was not affected (Extended Data Fig. 6c). Collectively, these data further support a model in which BRD4 promotes normal genome folding through a NIPBL interaction via the ET domain.

The ability of NIPBL to regulate genome folding is attributed to two, likely linked, mechanisms: facilitating loading of cohesin, which in turn extrudes chromatin loops to mediate interactions between distal regions[59,60]. Chromatin fractionation followed by immunoblotting for cohesin ring components upon BRD4 depletion did not reveal a change in the amount of cohesin bound to chromatin (Extended Data Fig. 7a). Therefore, we reanalyzed our Hi-C data to specifically capture features associated with loop extrusion. In particular, asymmetric enrichment signal on one edge of a TAD forms a "stripe". The stripe is postulated to form via a loop extrusion process and reflect an interaction of a single locus with a continuous segment of the genome. Consistent with previous reports[61], NIPBL and RAD21 occupancy was enriched at stripe anchors in DMSO-treated dTAG-BRD4 mESCs (Extended Data Fig. 7b). BRD4 was also enriched at stripe anchors (Extended Data Fig. 7b). Loss of *Nipbl* results in a dramatic reduction in loop extrusion using *in vitro* reconstitution assays[15]; consistently, we observed a ~3-fold reduction in the number of stripes upon BRD4 depletion (Extended Data Fig. 7c,d; Supplementary Table 3). Stripenn[62], an image-processing algorithm developed by our group, calculates a stripe score that integrates the contrast between the stripe and its background, pixel continuity within the stripe, and the median pixel intensity of the stripe. Regions identified as stripes in DMSO cells had a reduced stripe score and median pixel intensity upon BRD4 depletion (Extended Data Fig. 7e). We then assessed NIPBL occupancy in stripe domains and at regions previously identified as RAD21-NIPBL co-bound peaks, posited to represent cohesin-loading sites[61]. NIPBL occupancy was decreased at both RAD21-NIPBL co-bound peaks and NIPBL peaks within stripe domains (Extended Data Fig. 7f,g). Further, we assessed RAD21 occupancy from duplicate samples using CUT&RUN, which were processed as above. We observed a moderate reduction in RAD21 occupancy at RAD21-NIPBL peaks and at RAD21 peaks within stripe domains upon BRD4 depletion (Extended Data Fig. 7h,i). These data suggest BRD4-mediated NIPBL maintenance on chromatin impacts loop extrusion and RAD21 occupancy at RAD21-NIPBL sites and along stripe domains. Taken together, our data reveal that BRD4 mediates genome folding and higher-order chromatin organization.

Integrating transcription changes with altered architecture

BRD4 is a well-characterized transcription regulator[23], and we sought to understand the relationship between the architectural changes we observed and transcriptional changes

anticipated upon BRD4 depletion. Therefore, we assessed transcriptional dynamics in DMSO- and degron-treated cells using SLAM-seq, a technique that measures levels of newly transcribed mRNA based on 4-thiouridine incorporation[63]. As expected, SLAM-seq identified more changes in transcript levels compared to total RNA-seq (Fig. 6a). SLAM-seq identified 1,050 downregulated genes and 388 upregulated genes upon BRD4 depletion for 4.5 hours (n = 3 replicates; $|\log_2FC| > 1$, FDR < 0.05; Fig. 6a; Supplementary Tables 2 and 5). In addition, cohesin subunits were not differentially expressed (Supplementary Table 5). We calculated the percentage of genes that were dysregulated in individual TADs using SLAM-seq data. Dysregulated genes were most enriched in the deciles of TADs with greater interaction frequency changes upon BRD4 loss (Fig. 6b and Extended Data Fig. 7j). However, even amongst the TADs that lost the most interaction frequency upon BRD4 loss (top 10%, n = 480), 66% of the TADs (n = 317) did not contain any dysregulated genes, whether normalized to the number of genes (Fig. 6b) or TADs (Extended Data Fig. 7j) in each decile. Overall, we found that 3,896 TADs had no significantly dysregulated genes and 113 TADs contained no genes (Fig. 6b,c and Extended Data Fig. 7j). Furthermore, while we found an enrichment for differentially expressed genes closer to anchors of BRD4-sensitive versus BRD4-resistant loop anchors, the enrichment was not different from the underlying gene distribution (Extended Data Fig. 7k). The causal relationship between transcription and architecture is not clear[64], and while transcription may be an important regulator of short-range gene-level contacts[65], our data indicate that local transcriptional changes across the genome are unlikely sufficient to drive the BRD4-dependent effects on TADs and loops revealed in this study.

BRD4-NIPBL interaction promotes neural crest differentiation

Our data reveal a necessity for BRD4 in neural crest development and underscore the importance of the BRD4-NIPBL interaction in genome organization. Therefore, we sought to understand if loss of the BRD4-NIPBL interaction was responsible for any phenotype we observed in the neural crest-BRD4 model. A subset of cardiac neural crest contribute to the smooth muscle surrounding the aortic arch arteries, and outflow tract abnormalities mediated by aberrant neural crest are often associated with smooth muscle differentiation defects[66,67]. Smooth muscle was reduced around the aortic arch arteries of E11.5 *Brd4^{f/f}, Wnt1*Cre+, *R26^{mt-mg/+}* embryos compared to *Brd4^{f/+}, Wnt1*Cre+, *R26^{mt-mg/+}* littermates (Fig. 7a). This was accompanied by a reduction in neural-crest-derived smooth muscle around the aorta and pulmonary artery in E14.5 *Brd4^{f/f}, Wnt1*Cre+, *R26^{mtmg/+}* embryos compared to *Brd4^{f/+}, Wnt1*Cre+, *R26^{mt-mg/+}* littermates (Fig. 7b). In order to validate and extend these results, we turned to an *in vitro* differentiation system with the aforementioned murine neural crest progenitor cell line (O9–1).

We differentiated neural crest progenitor cells into Smooth Muscle Actin (SMA)+ smooth muscle cells using established protocols[33] (Fig. 7c). SMA+ cells were spindle-shaped with visible stress fibers. Loss of BRD4 led to a reduction of progenitor differentiation into smooth muscle (Fig. 7c and Extended Data Fig. 8a,b). Next, we depleted endogenous *Brd4* using shRNA, while simultaneously expressing wildtype or mutant versions of GFP-hBRD4 resistant to shRNA targeting murine *Brd4*. We optimized transfection and infection conditions to ensure expression levels of GFP-hBRD4 constructs were comparable

to endogenous BRD4 (Fig. 7c and Extended Data Fig. 8a). Expression of wildtype GFP-hBRD4 maintained a normal number of SMA$^+$ cells despite knockdown of endogenous *Brd4* (Fig. 7c). In contrast, introduction of NIPBL-binding-defective hBRD4 mutants did not rescue smooth muscle differentiation (Fig. 7c). Expression of two smooth muscle markers, *Cnn1* and *Acta2*, largely mirrored these results (Extended Data Fig. 8c). Additionally, *Brd4* knockdown did not affect *Nipbl* expression (Extended Data Fig. 8d). These data indicate that the ET domain of BRD4 is required for neural crest progenitor differentiation into smooth muscle.

Consistent with the critical nature of the BRD4-NIPBL interaction, shRNA-mediated knockdown of *Nipbl* also impeded smooth muscle differentiation (Fig. 7d and Extended Data Fig. 8e,f). To further understand whether the smooth muscle differentiation defects produced by loss of BRD4 were due to change in cohesin function, we sought to rescue differentiation by manipulating other cohesin regulators. A previous study demonstrated that changes in genome organization, including chromatin looping, resulting from NIPBL depletion can be partially rescued by simultaneous depletion of WAPL, a negative cohesin regulator[25–28]. We found that simultaneous depletion of WAPL and NIPBL rescued the percentage of SMA$^+$ cells differentiated from neural crest progenitors compared to NIPBL depletion alone (loss of WAPL alone had a relatively minor effect; Fig. 7d and Extended Data Fig. 8e,f), suggesting that NIPBL promotes smooth muscle differentiation by modulating cohesin function. Strikingly, simultaneous depletion of WAPL and BRD4 also rescued the percentage of SMA$^+$ cells differentiated from neural crest progenitors compared to BRD4 depletion alone (Fig. 7d and Extended Data Fig. 8e). SMA$^+$ cells adopted the typical morphology of spindle-shaped smooth muscle cells with visible stress fibers (Fig. 7d, insets), and expression of *Cnn1* and *Acta2* were consistent with these results (Extended Data Fig. 8g,h). Taken together, these studies suggest that BRD4 regulates genome folding through NIPBL binding, and our data are consistent with a critical functional role for this interaction in neural crest differentiation into smooth muscle cells.

Discussion

BRD4 has been described as a 'cellular Swiss army knife', with the ability to mediate transcriptional pause-release, act as a histone acetyltransferase, bind regulatory elements and recruit transcriptional machinery[23]. We reveal yet another role: BRD4 is a positive meditator of NIPBL and thereby maintains genome folding (Fig. 8). Acute loss of BRD4 weakens loop and intra-TAD interactions at specific areas across the genome and the architectural defects are at least partially attributed to a loss of BRD4-NIPBL interaction. Accordingly, loss of BRD4 in neural crest cells *in vivo*, phenocopies mutations in *NIPBL*, which are also often observed in human cohesinopathies. The ability to acutely degrade BRD4 in less than a cell cycle in a non-differentiating pool of cells allowed for assessment of BRD4 loss independent of biases arising from changes in cellular identity. Extending these findings, our data suggest that one physiologic role of the BRD4-NIPBL interaction is to mediate normal smooth muscle differentiation of neural crest cells. Even more striking, depletion of the negative cohesin regulator WAPL is sufficient to rescue smooth muscle differentiation in cells with BRD4 depletion. This rescue further demonstrates the critical role that BRD4 plays in mediating cohesin function. Together, this study illustrates the functional relevance

of genome folding, and specifically the importance of properly balancing the positive and negative effectors of cohesin function in cellular differentiation. Due to space constraints, we discuss the relevance of our data on understanding the cellular basis of cohesinopathies and the implications for developmental competence in the Supplemental Discussion. We also place our findings in context of recent studies depleting cohesin (and related) proteins and how our data support and extend the loop extrusion model in the Supplemental Discussion.

Methods

Mice

Brd4 floxed mice were obtained from Keiko Ozato's laboratory[30], and *Wnt1*Cre mice were obtained from Jackson Laboratories (#022137). *R26mt-mg* mice were obtained from Jackson Laboratories[68]. Mice were maintained on mixed CD1/B6/129 genetic backgrounds. Littermate embryos were analyzed in all experiments unless otherwise noted. The Institutional Animal Care and Use Committee approved all animal protocols.

Tissue immunohistochemistry and immunofluorescence

Mice were dissected and embryos were harvested at E11.5, E12.5, E14.5, E16.5 and E17.5. All embryos were fixed in 2% paraformaldehyde in PBS (Sigma #P6148) overnight at 4°C on a tilting shaker set at low speed. Following fixation, the embryos were dehydrated with an ethanol gradient (30% ethanol for 2 hours, 50% ethanol for 2 hours, 70% ethanol for 2 hours, 95% ethanol overnight and 100% ethanol overnight). Dehydrated embryos were perforated, cleared with xylene, embedded in paraffin blocks, and sectioned into 7 μm thick segments.

Gross tissue morphology was examined by Hematoxylin and Eosin (H/E) staining following standardized methods of the University of Pennsylvania Histology and Gene Expression Co-Op (https://www.med.upenn.edu/cvi/histology-and-gene-expression-co-op.html)[69]. Collagen and extracellular matrix deposition, bone mineralization and smooth muscle morphology was assessed by Masson Trichrome Staining according to standard protocol of the University of Pennsylvania Histology and Gene Expression Co-Op. All slides were imaged at 2× or 4× magnification on the Nikon Eclipse 80i fluorescence microscope.

Sections analyzed by immunofluorescence were stained per the optimized and standardized methods of the University of Pennsylvania Histology and Gene Expression Co-Op. Briefly, slides were brought to room temperature, deparaffinized with xylene, and rehydrated through a series of steps (100% ethanol for 2 minutes, 95% ethanol for 2 minutes, ddH$_2$O for 2 minutes twice). Tissue sections were blocked and permeabilized in 10% normal serum in PBS + 0.5% Tween-20, after which the slides were incubated with designated primary antibodies overnight at 40°C. Following four washes with 0.1% PBS Tween-20 for 5 minutes at room temperature, corresponding secondary antibodies were added, incubated for an hour at room temperature, and washes were performed as above. Slides were mounted with VectaShield with DAPI (Vector Laboratories #H-2000) mounting medium and scanned on the Aperio ScanScope IF (Leica Biosystems) at 20× magnification. Areas populated by neural crest derivatives were manually outlined and the number of DAPI$^+$, Wnt1$^+$(GFP$^+$)

and phospho-histone $H3^+$ were quantified using certain features on Image J. At least two embryos (approximately 30–37 frontal sections in total) were quantified per genotype. Proliferation indices were calculated as percentage of DAPI and Wnt1 positive cells at E11.5. Statistical significance between genotypes was calculated using GraphPad Prism v9 (GraphPad Software Inc., USA).

Primary antibodies and dilutions used: Goat polyclonal anti-GFP (1:100, Abcam #ab6673 Lot#GR3213188–14), Rabbit polyclonal anti-BRD4 (1:2,000, Bethyl #A301–985A100 Lot#7), Rabbit polyclonal anti-phospho-histone H3 (Ser10) (1:20, Cell signaling #9710L), Mouse monoclonal anti-alpha smooth muscle actin (1:200, Sigma #A5228 Lot#065M4762V). Antigen retrieval was used for all primary antibodies except for anti-alpha smooth muscle actin. Secondary antibodies and dilutions used: Alexa fluor 555 donkey anti-rabbit IgG(H+L) (1:250, Invitrogen #A31572 Lot#2088692) and Alexa fluor 488 donkey anti-goat IgG(H+L) (1:250, Invitrogen #A11055 Lot#2059218).

Cell culture

HEK293T cells were purchased from ATCC (#CRL-11268) and maintained at 37°C in 20% O_2 and 5% CO_2 in DMEM supplemented with 10% fetal bovine serum (FBS) and 1% penicillin, and streptomycin. mESCs (ATCC #CRL-1934) were maintained at 37°C in 20% O_2 and 5% CO_2 on gelatin-coated plates in knock-out DMEM (Gibco #10829018), 10% knockout serum replacement (Gibco #10828028), 1% FBS (Hyclone #SH30070.03), 1× non-essential amino acids (Gibco #11140050), 2 mM L-glutamine (Gibco #25030081), 1% ITS-X supplement (Gibco #51500056), 55 μM β-mercaptoethanol (Gibco #21985023), 1×10^3 units/ml recombinant mouse LIF (Millipore #ESG1107), 3 μM GSKβ inhibitor CHIR99021 (Reprocell #04–0004-02), 1 μM MEK inhibitor PD0325901 (Reprocell #04–0006-02), and 1% penicillin and streptomycin. For the O9–1 neural crest cell line (Sigma #SCC049), cells were cultured in basal medium (DMEM, 15% FBS, 0.1 mM non-essential amino acids, 1 mM sodium pyruvate (Gibco #11360070), 55 μM β-mercaptoethanol, 100 U/ml penicillin, 100 μg/ml streptomycin, and 2 mM L-glutamine) previously conditioned by STO feeder cells for 24 hours. The medium was filtered using a 0.22-μm PES membrane (Millipore #SCGP00525) and supplemented with 25 ng/ml basic fibroblast growth factor (R&D systems #233-FB-025) and 1×10^3 units/ml recombinant mouse LIF. To induce smooth muscle cell differentiation, O9–1 cells were cultured in differentiation medium (DMEM, 10% FBS, 100 U/ml penicillin, and 100 μg/ml streptomycin) for two days (for RT-qPCR and IF experiments) and three days (for western blotting experiments) to assess differentiation markers. dTAG-13 (Sigma #SML2601), dTAG^v-1 (a gift from the Nathanael Grey's laboratory) and MZ3 (a gift from Thomas Ciulli's laboratory) were treated at appropriate concentration and time as indicated in the figures.

Immunofluorescence

Cells were fixed with 2% (O9–1 cells) or 4% (mESCs) PFA (Electron Microscopy Sciences #15710) for 10 minutes, washed twice with phosphate buffered saline (PBS) for 5 minutes, permeabilized with 0.5% triton X-100/PBS for 5 minutes, and washed twice with PBS for 5 minutes. All steps were performed at room temperature. Cells were then incubated with blocking solution (3% BSA and 0.02% Tween-20 PBS) for an hour at room temperature,

followed by overnight incubation with primary antibody in blocking solution at 4°C. The antibodies used were anti-BRD4 (1:100, Bethyl Laboratories #A301–985A100 Lot#7), anti-GFP (1:100, Abcam #ab290), anti-OCT4 (1:200, Abcam #ab19857 Lot#GR3173193–1) and Cy3 conjugated SMA antibody (1:5,000, anti-actin alpha-smooth muscle-Cy3, Sigma #C6198). The following day, cells were washed three times with 0.02% Tween-20/PBS for 5 minutes, and incubated with secondary antibodies [Goat anti-Rabbit IgG Secondary Antibody, Alexa Fluor Plus 488 (1:1,000, Thermo Fisher #A32731 Lot#VG302077) and 555 (1:1,000, Thermo Fisher #A32732 Lot#VG308859) and Goat anti-Mouse IgG Secondary Antibody, Alexa Fluor Plus 488 (1:1,000, Thermo Fisher # A10680 Lot#2064014) and 555 (1:1,000, Thermo Fisher #A32727 Lot#UL287768)] for 2 hours at room temperature. Cells were washed three times with PBST (0.1% Tween-20 in PBS) for 5 minutes. Nuclear staining was carried out with incubation of DAPI (1:5,000 in PBS), for 5 minutes, followed by three 5 min washes in PBST. Samples were mounted with SlowFade™ Gold Antifade Mountant (Fisher #S36936). Images were obtained with Leica SP8 confocal microscope using 63×/1.40 oil objective or with Leica widefield DMi8 microscope using 10× objective. For SMA$^+$ and BRD4$^+$ cell quantification, we used at least 3 biological replicates per condition, and imaged more than three random fields per sample. The images were then semi-automatically processed in ImageJ v1.53c by thresholding each antibody signal and quantifying unique segmentations per nuclear mask. The statistical analysis of the cell counts was performed in GraphPad Prism v9.

Oligopaints FISH

Adherent dTAG-BRD4 cells were harvested using Accutase solution (Sigma #A6964), washed twice in PBS for 5 minutes, fixed for 10 minutes in 4% paraformaldehyde (Thermo Fisher #15713S) in PBS with 0.05% Tween-20, followed by three washes in PBS for 5 minutes each. Cells were then settled on poly-L-lysine-treated glass slides for 30 minutes at room temperature and stored in PBS at 4°C until ready to use. Hybridization steps were performed directly on the slides, as previously described[58] with some modifications. Cells were permeabilized in 0.5% Triton-PBS for 15 minutes. Slides were then incubated in 2× SSCT (0.3 M NaCl, 0.03 M sodium citrate and 0.1% Tween-20) for 5 minutes at room temperature, 2× SSCT/50% formamide (Thermo Fisher #BP227500) for 5 minutes at room temperature, and 2× SSCT/50% formamide for 20 minutes at 60°C. Hybridization mix [50 μM of Oligopaints FISH probes (50 pmol of probes in 25 μl total volume), 10% dextran sulfate, 2× SSCT/50% formamide, 4% polyvinylsulfonic acid (PVSA), 5.6 mM dNTPs and 10 μg RNase, was added to the slides and covered with coverslip. Slides were then denatured on a heat block at 80°C for 30 minutes, and then incubated at 37°C overnight in a humidified chamber. The next day, the coverslip was removed, and the slides were washed in 2× SSCT at 60°C for 15 minutes, 2× SSCT at room temperature for 10 minutes, and 0.2× SSC at RT for 10 minutes. Next, hybridization buffer (10% dextran sulfate, 2× SSCT, 10% formamide and 4% PVSA) containing secondary probes conjugated to fluorophores (10 pmol per 25 μl buffer) was added to slides and covered with a coverslip. Slides were placed in a humidified chamber and incubated for 2 hours at room temperature. Slides were washed in 2× SSCT at 60°C for 15 minutes, 2× SSCT at room temperature for 10 minutes, and 0.2× SSC at room temperature for 10 minutes, and then the DNA was stained with Hoechst (1:10,000 in 2×

SSC) for 5 minutes. Slides were then mounted in SlowFade Gold Antifade (Thermo Fisher #S36936).

Cleavage Under Target and Release (CUT&RUN)

The CUT&RUN protocol was performed in triplicate for BRD4 and NIPBL and duplicate for H3K27ac and RAD21, and performed as previously described[70] with modifications. Briefly, 5×10^6 mES cells per well were treated with 500 nM of dTAG-13 or DMSO and harvested at 4.5 hour. Following treatment, cells were harvested via gentle agitation post the incubation with Accutase for 5 minutes and collected via centrifugation at 300 g for 3 minutes at 4°C. The cells were washed twice with ice-cold PBS and nuclei were isolated with Nuclear extraction buffer [20 mM HEPES-KOH, pH 7.9, 10 mM KCl, 0.5 mM Spermidine (Sigma #05292–1ml-F), 0.1% Triton X-100, 20% Glycerol and 1× protease and phosphatase inhibitor (Thermo Fisher #78442)]. To aid in nuclear capture, isolated nuclei were incubated with activated Concanavalin A beads (Bangs Laboratories #Bp531) for 15 minutes at room temperature followed by incubation with the desired primary antibody (1:100 dilution) overnight. Any unbound antibody was washed away using Wash Buffer (20 mM HEPES-NaOH pH 7.5, 150 mM NaCl, 0.5 mM Spermidine, 1× protease phosphatase inhibitor) for a total of two washes. Supernatant was discarded via bead liquid separation using a magnetic stand and pA-MNase was added at a final concentration of 700 ng/ml (Batch 6: Stock concentration: 143 μg/ml) and the complex was incubated for 1 hour at 4°C. Following incubation, the bound complexes were washed twice with Wash Buffer and placed in a 0°C metal block for 5 minutes to pre-chill the tubes. To activate pA-MNase, $CaCl_2$ was added to the pre-chilled bound complexes at a final concentration of 2 mM and incubated in the 0°C metal block for 30 minutes. The digestion reaction was neutralized by the addition of an equal volume of 2× STOP buffer (200 mM NaCl, 20 mM EDTA, 4 mM EGTA, 50 μg/ml RNase A, 40 μg/ml glycogen and 100 pg/ml heterologous spike in DNA) followed by incubation at 37°C for 10 minutes to released cleaved fragments of DNA. The targeted protein-DNA complex was released via centrifugation at 16,000 g for 5 minutes and supernatant was collected and transferred to freshly labelled 1.7 ml tubes. Depending on whether the targeted proteins were nucleosomal or transcription factors, the digested DNA was purified either via spin column or phenol chloroform. For H3K27ac, a method of spin column method (Macherey-Nagel #740609.250) of extraction was followed according to the manufacturer's instructions to recover large DNA-protein complexes. To enrich for smaller fragments occupied by non-histone proteins (BRD4, NIPBL and RAD21), a phenol chloroform extraction protocol was followed as briefly described. The supernatant was decanted into a fresh tube to which 10% SDS (final concentration 0.1%) and proteinase K (final concentration of 20 mg/ml) was added and mixed by inversion followed by incubation for 10 minutes at 70°C. Post incubation, phenol-chloroform-isoamyl alcohol was added to the solution and vortexed at full speed to mix. The solution was transferred to a phase lock tube, centrifuged at 16,000 g for 5 minutes and inverted 10 times post the addition of chloroform followed by another round of centrifugation at 16,000 g for 5 minutes. The supernatant was transferred to a fresh tube containing glycogen (final concentration 20 μg/ml) and DNA was precipitated via the addition of 100% ethanol. The samples were incubated on ice for 10 minutes and subsequently centrifuged at 16,000 g at 4°C. Excess liquid was carefully discarded and 1 ml of ethanol was added to the pellet and

tubes were mixed by inverting. Samples were centrifuged once again at 16,000 g at 4°C. The supernatant was carefully discarded, and the pellet was air dried for 10 minutes and resuspended in a desired amount of TE buffer (1 mM Tris-HCl pH 8, 0.1 mM EDTA). DNA concentration following both methods of extraction was estimated using the Qubit and quality was assessed prior to library preparation using the Agilent BioAnalyzer 2100 (Agilent Technologies, USA) using the High Sensitivity DNA Kit (Agilent Technologies #5067–4626). The antibodies used were, Rabbit polyclonal anti-BRD4 [Bethyl Laboratories #A301–985A100 (Lot 7)], Rabbit Polyclonal Anti-NIPBL [Bethyl Laboratories #A301–779 (Lot 4)], Rabbit polyclonal anti-H3K27ac (Abcam #Ab4729), Rabbit polyclonal anti-RAD21 (Abcam #Ab992), normal rabbit IgG (Cell signaling #2729S).

SLAM-seq

The SLAM-seq protocol was carried out as described in the SLAM-Seq Anabolic Kinetics Kit user guide (Lexogen #061.24) with modifications. Briefly, mESCs were seeded in 0.1% bovine gelatin (Sigma #G9391–500g) coated 6-well plates approximately two days prior to S4U labelling in order to attain an optimum confluency of around 70–80% (~2×10^6 cells). All conditions were set up in triplicate. On the day of labelling, mESC medium was aspirated and refreshed with pre-warmed mESC growth medium containing either 500 nM dTAG-13 or DMSO to pre-establish acute degradation of BRD4. Time course for BRD4 degradation was set at 4.5 hours. Fifteen minutes into the time course, newly synthesized RNA was labelled via the addition of 4-thiouridine to all wells, including controls, at a final concentration of 500 μM/well and metabolic labelling was continued until the end of the time course. For the 4.5 hour time point, S4U medium was refreshed after 3 hours to continue efficient labelling. At the respective time points, medium was aspirated and mESCs were harvested following the addition of 400 μl of Accutase. The single-cell suspension from each well was transferred into corresponding tubes and centrifuged at 2,500 rpm for 5 minutes to pellet cells. The cell pellet was washed twice with ice-cold 1× PBS and RNA extraction was carried out using the RNeasy Plus kit (Qiagen #74134). Recommended amount of reducing agent (as indicated in the manufacturer's protocol) was added to all extraction buffers to maintain a reducing environment during extraction. 8 μg of total RNA was alkylated via treatment with 10 mM iodoacetamide (IAA) at 50°C for 5 minutes under optimal reaction conditions and purified by ethanol precipitation. IAA fixed RNA concentrations were estimated using the Nanodrop and approximately ~300 ng/μl of alkylated RNA per sample was sent to Lexogen for downstream processing and sequencing. On arrival, RNA concentration and quality were assessed via the Nanodrop. Subsequently, RNA integrity was assessed on the Agilent Bioanalyzer (Agilent Technologies, USA), prior to library preparation, using the RNA 6000 Nano Assay Kit (Agilent Technologies #5067–1511).

In-situ Hi-C

The in-situ Hi-C protocol was carried out as previously described[7] with modifications. Briefly, mESCs were seeded in 0.1% bovine gelatin (Sigma #G9391–500g) coated 6-well plates approximately three days prior to harvest in order to attain an optimum confluency on the day of harvest. All conditions were set up in duplicate. On the day of harvest, mESC medium was aspirated and refreshed with pre-warmed mESC growth medium containing

either 500 nM dTAG13 or DMSO to establish acute degradation of BRD4 for a time course of 4.5 hours. Following treatment, mESC medium was aspirated and cells were harvested following the addition of 400 μl of Accutase. The single-cell suspension from each well was transferred into their respective tubes and centrifuged at 2,500 rpm for 5 minutes. The resulting cell pellet was washed twice with ice-cold 1× PBS and aliquot into separate tubes containing 1.5×10^6 cells each (per well/per condition). Cells were briefly centrifuged at 2,500 rpm at 4°C for 5 minutes and the supernatant was discarded. The cell pellet containing 1.5×10^6 cells was resuspended and crosslinked in 1% formaldehyde (Thermo Fisher #28906) for 12 mins. The crosslinking reaction was quenched by the addition of 2.5 M glycine (final concentration 0.2 M) (Thermo Fisher #15527013) followed by incubation for 5 minutes. Crosslinked cells were pelleted via centrifugation at 2,500 rpm at 4°C for 5 minutes and the supernatant was discarded. Cells were resuspended and washed twice with ice-cold 1× PBS and to remove all traces of formaldehyde. Cell pellets were flash frozen and stored at −80°C until required for downstream processing. Frozen cell pellets were shipped on dry ice to the Genome Technology Center at NYU Langone Health, NY. All subsequent processing, quality control and sequencing of samples was carried out at the Genome Technology Center.

Quantification and Statistical analysis

All statistical comparisons were performed in R v3.5.2 or GraphPad Prism v9 as specified in the relevant figures and corresponding methods sections. Normality of the data was assessed visually with QQplots and formally using the Shapiro-Wilk test in R as indicated. Quality control of sequenced reads was performed by FastQC (https://github.com/s-andrews/FastQC) and MultiQC (https://github.com/ewels/MultiQC). Correlation between mapped reads from biological replicates was assessed in deepTools v3.1.3 using the Spearman method.

Data Availability

All data generated for this paper have been deposited at NCBI Gene Expression Omnibus (GEO; http://www.ncbi.nlm.nih.gov/geo/) and are available under accession number GSE169516. Mouse genome sequence mm10: http://ftp.ebi.ac.uk/pub/databases/gencode/Gencode_mouse/release_M10/GRCm38.primary_assembly.genome.fa.gz

*Saccharomyces cerevisiae* genome sequence sacCer3:

https://hgdownload.soe.ucsc.edu/goldenPath/sacCer3/bigZips/sacCer3.fa.gz

BRD4 ChIP-seq: http://dc2.cistrome.org/api/hgtext/34084/?db=mm10

NIPBL ChIP-seq: http://dc2.cistrome.org/api/hgtext/2864/?db=mm10

H3K27ac ChIP-seq: http://dc2.cistrome.org/api/hgtext/67169/?db=mm10

RAD21 ChIP-seq: http://dc2.cistrome.org/api/hgtext/39300/?db=mm10

Code Availability

OligoMiner is available at https://github.com/beliveau-lab/OligoMiner. cLoops is available at https://github.com/YaqiangCao/cLoops. TADtool is available at: https://github.com/vaquerizaslab/tadtool. Juicer Tools is available at https://github.com/aidenlab/juicer. Other tools used are indicated in the Methods sections. We utilized existing published analysis tools as indicated above. No new analysis tools were generated, and scripts employed to analyze the data using the published tools are available upon request.

Extended Data
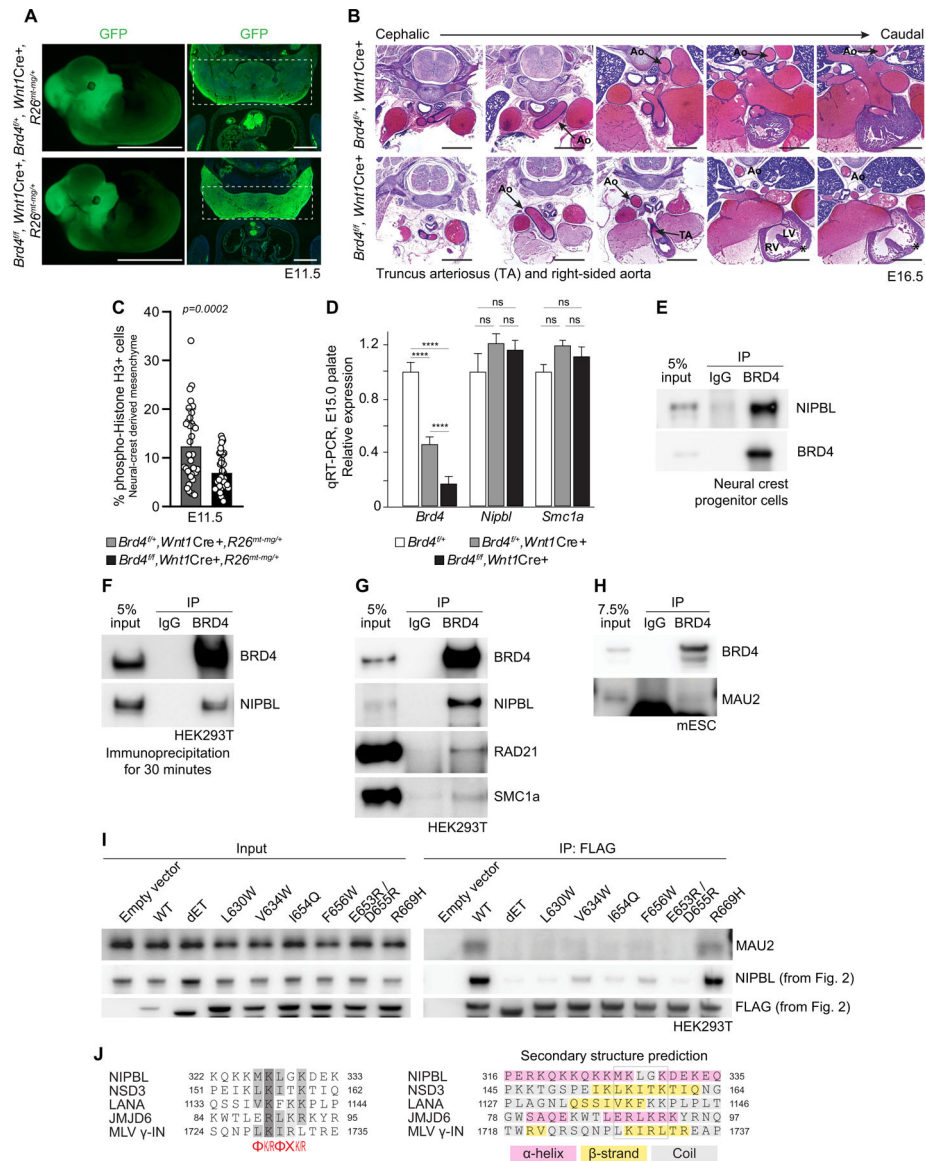
Extended Data Fig. 1. Characterization of BRD4 in neural crest and the interaction with NIPBL
(**A**) GFP epifluorescence and immunohistochemistry (coronal section) of E11.5 *Brd4^{f/f}*, *Wnt1*Cre+, *R26^{mt-mg/+}* and *Brd4^{f/+}*, *Wnt1*Cre+, *R26^{mt-mg/+}* embryos. Scale bar,

epifluorescence: 500 mm; immunohistochemistry: 500 μm. **(B)** Multiple sections of E16.5 *Brd4*$^{f/f}$, *Wnt1*Cre+ and *Brd4*$^{f/+}$, *Wnt1*Cre+ embryo showing outflow tract and heart. Mutant demonstrates right-sided aortic arch and truncus arteriosus. (Ao, Aorta; RV, right ventricle; LV, left ventricle; TA, truncus arteriosus). Second image duplicated from Fig. 1. (* denotes sectioning artifact). Scale bar, 1 mm. **(C)** Percentage of phospho-Histone H3+ cells in neural crest-derived craniofacial mesenchyme (each point represents one field of view, 35 (*Brd4*$^{f/+}$, *Wnt1*Cre+, *R26*$^{mt-mg/+}$) and 37 (*Brd4*$^{f/f}$, *Wnt1*Cre+, *R26*$^{mt-mg/+}$) fields of view total from two embryos, mean and SD shown, student's T-test). **(D)** Expression of indicated genes in E15.0 secondary palate tissue (Unpaired T-test; ****p<0.0001. Error bars denote SEM). Gene expression normalized to the expression of *Hprt1*. **(E)** Immunoprecipitation of endogenous BRD4 blotted for BRD4 and NIPBL (murine neural crest cells, O9–1 cells). **(F)** Immunoprecipitation (30 minutes) of endogenous BRD4 from and blotted for BRD4 and NIPBL (HEK293T cells). **(G)** Immunoprecipitation of endogenous BRD4 and blotted for indicated proteins (HEK293T cells). **(H)** Immunoprecipitation of endogenous BRD4 and blotted for indicated proteins (mESCs). **(I)** Indicated FLAG-tagged versions of BRD4 immunoprecipitated (HEK293T cells). Immunoblots probed with indicated antibodies. The NIPBL and FLAG immunoblots are reproduced from Fig. 2e as the proteins were all blotted for from the same blot. **(J)** Alignment of BRD4-interacting peptides of NSD3, LANA, JMJD6 and MLV-γ-integrase and putative BRD4-interacting peptide of NIPBL. Residues highlighted by gray are conserved across other peptides. Consensus motif indicated at the bottom (Φ represents a hydrophobic amino acid and X any amino acid). Predicted α-helix, β-strand and coil structures are marked by pink, yellow and gray color, respectively. Predictions based on PSPIRED[71]. The consensus motif is highlighted in the gray box.
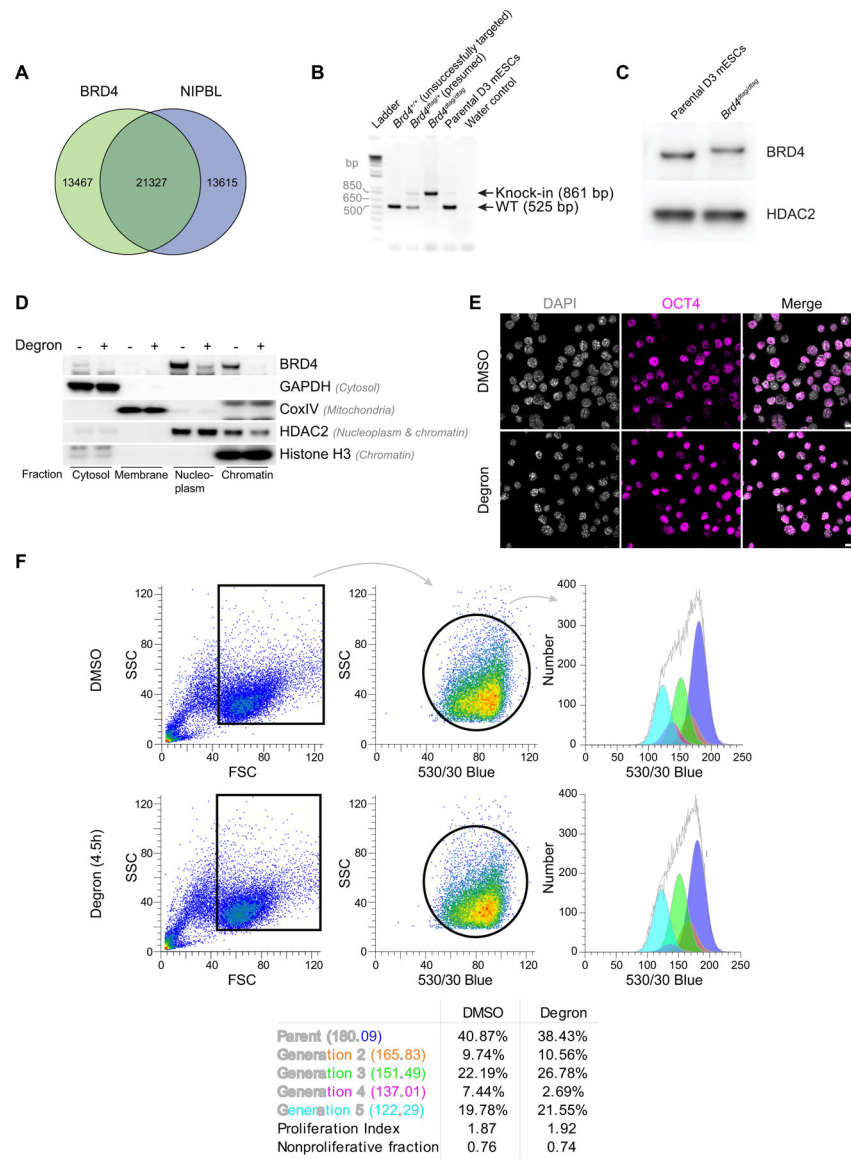
Extended Data Fig. 2. Generation of dTAG-BRD4 mouse embryonic stem cell line
(**A**) Venn diagram showing the comparison of BRD4 and NIPBL peaks. (**B**) PCR of genomic DNA from clones of indicated genotype using oligos annealing outside of area of homologous recombination. "Unsuccessfully targeted" is a line which was targeted by sgRNA and Cas9, but dTAG was not inserted. Of clones shown, only $Brd4^{dtag/dtag}$ was confirmed by Sanger sequencing. (Ladder: Thermo, #10787–018). (**C**) Immunoblot of chromatin fraction from parental and dTAG-BRD4 mESCs. (**D**) Confirmation of fractionation protocol. Cytosol, membrane, nucleoplasm, and chromatin fractions from dTAG-BRD4 mESCs in control and the degron conditions were blotted for indicated proteins. (**E**) OCT4 immunofluorescence from dTAG-BRD4 mESCs in control and the degron conditions. Scale bar, 20 μm. (**F**) Flow cytometry-based analysis of proliferation/ doubling time using CellTrace CFSE at 4.5 hours post treatment with DMSO or 500 nM dTAG-13. Rectangle and circle in left and middle graphs indicates gate in which cells

analyzed using Cell Proliferation tool on ModFIT LT v5.0 (n=23823 and 23859 cells in DMSO and Degron, respectively).
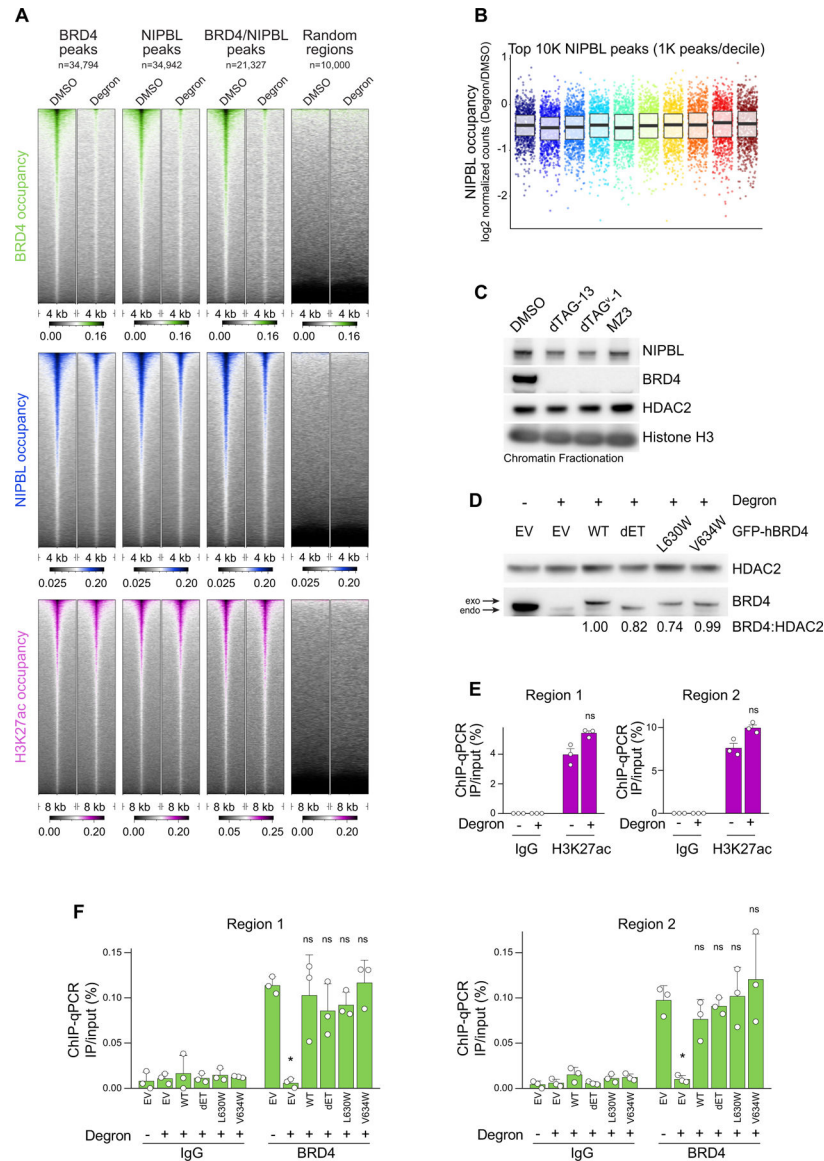
Extended Data Fig. 3. BRD4 regulates NIPBL occupancy

(**A**) Co-occupancy analysis of BRD4 (green), NIPBL (blue) and H3K27ac (purple) at BRD4, NIPBL, or BRD4/NIPBL peaks as defined in Extended Data Fig. 2a. (**B**) NIPBL occupancy [log2 normalized counts (Degron/DMSO)] across top 10K peaks. (**C**) Immunoblot of chromatin fractionations from DMSO, dTAG-13 (500 nM), dTAG^v-1 (500 nM), and MZ3 (1 μM)-treated cells for 4.5 hours for indicated proteins. The samples were derived from the same experiment and blots were processed in parallel. (**D**) Expression of indicated BRD4-mutants in dTAG-BRD4 mESCs upon degradation of endogenous BRD4. HDAC2 is used as a loading control. Relative band intensity ratio (BRD4:HDAC2) is indicated. (**E**) ChIP-qPCR of H3K27ac at regions indicated in Fig. 3e. Two-tailed T-test was used for

comparison. Error bars denote the mean + SEM. **(F)** ChIP-qPCR of BRD4 or IgG at the same two regions assayed in Fig. 3f. One-way ANOVA Dunnett's test was used to compare conditions to empty vector transfection with DMSO treatment. *p<0.05. Error bars denote the mean + SD.
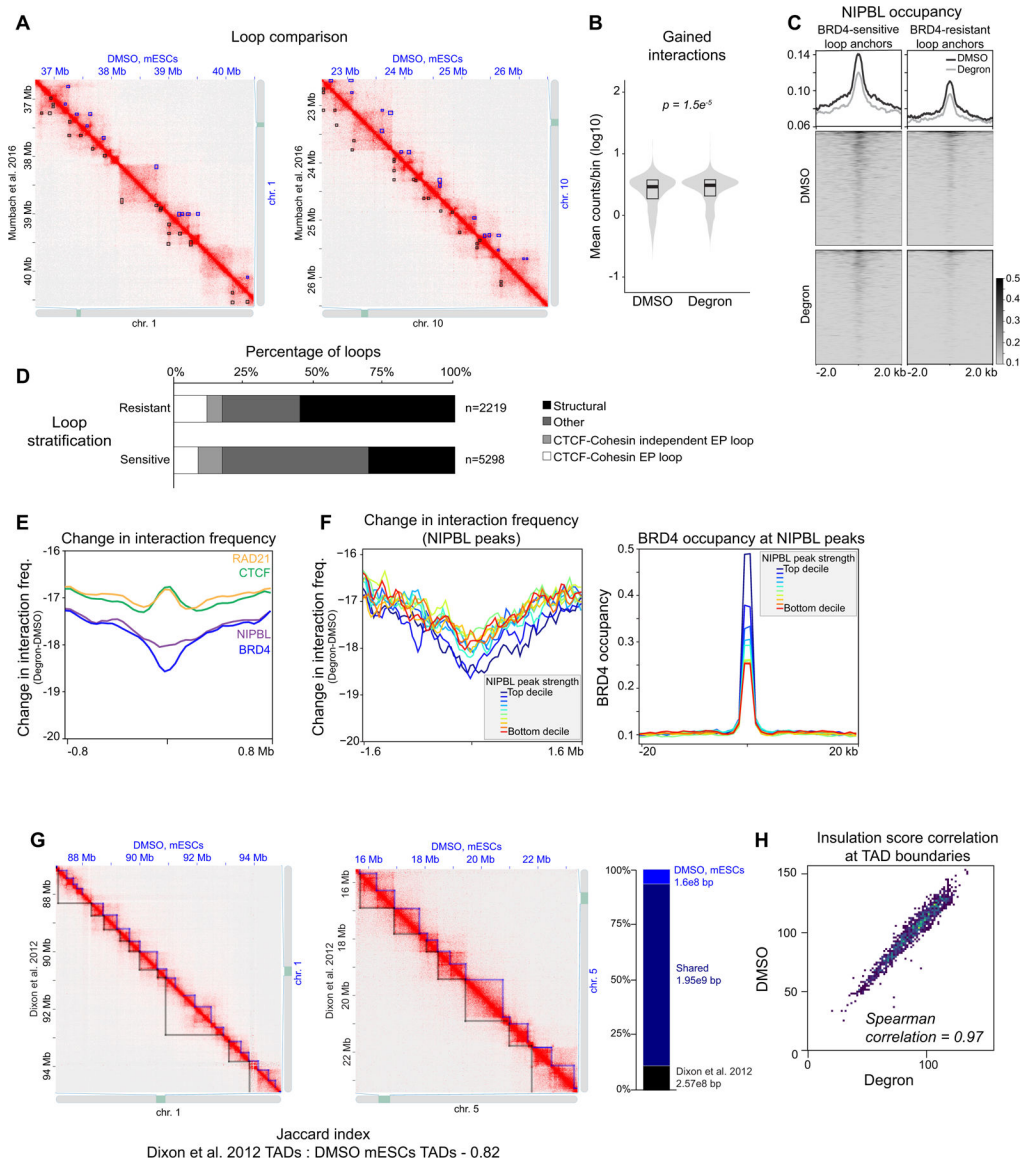
Extended Data Fig. 4. BRD4 maintains higher order chromatin structure
(A) Hi-C matrix comparing c-loop identified loops in DMSO, dTAG-BRD4 mESCs (blue) to mESCs profiled in Mumbach et al., 2016 (black) at two different regions. **(B)** Mean counts/bin of gained interactions in DMSO and the degron conditions. T-test used for comparison. **(C)** NIPBL occupancy at BRD4-sensitive and -resistant loop anchors in DMSO and the degron conditions. **(D)** Stratification of BRD4-resistant and -sensitive loops. Structural loops refer to loops with CTCF and RAD21 peaks at both anchors and 0–1 anchors have H3K27ac peak. CTCF-Cohesin enhancerpromoter (EP) loops refer to loops

with H3K27ac, CTCF and RAD21 peaks at both anchors. CTCF-Cohesin independent loops refer to loops with CTCF and RAD21 peaks at 0–1 anchors and both anchors have H3K27ac peak. Other refers to all loops which do not fall into these categories. Anchor regions were extended by 15 kb upstream and downstream for peak intersections. **(E)** Change in interaction frequency at BRD4, NIPBL, RAD21, and CTCF peaks. **(F)** Change in interaction frequency at NIPBL peaks (stratified into deciles of peak strength) upon depletion of BRD4 (left) and BRD4 occupancy (normalized counts) at NIPBL peaks (right) (stratified into deciles of peak strength). **(G)** Hi-C matrix comparing TADs in DMSO, dTAG-BRD4 mESCs (blue) to mESCs profiled in Dixon et al., 2012 (black) at two different regions. Adjacent bar plot compares the percentage of basepairs uniquely found in a TAD in DMSO, dTAG-BRD4 mESCs (light blue), Dixon et al., 2012 mESCs (black) or shared between the datasets (navy). Jaccard index between datasets 0.82. **(H)** Correlation of insulation score specifically at TAD boundaries between DMSO and the degron conditions.
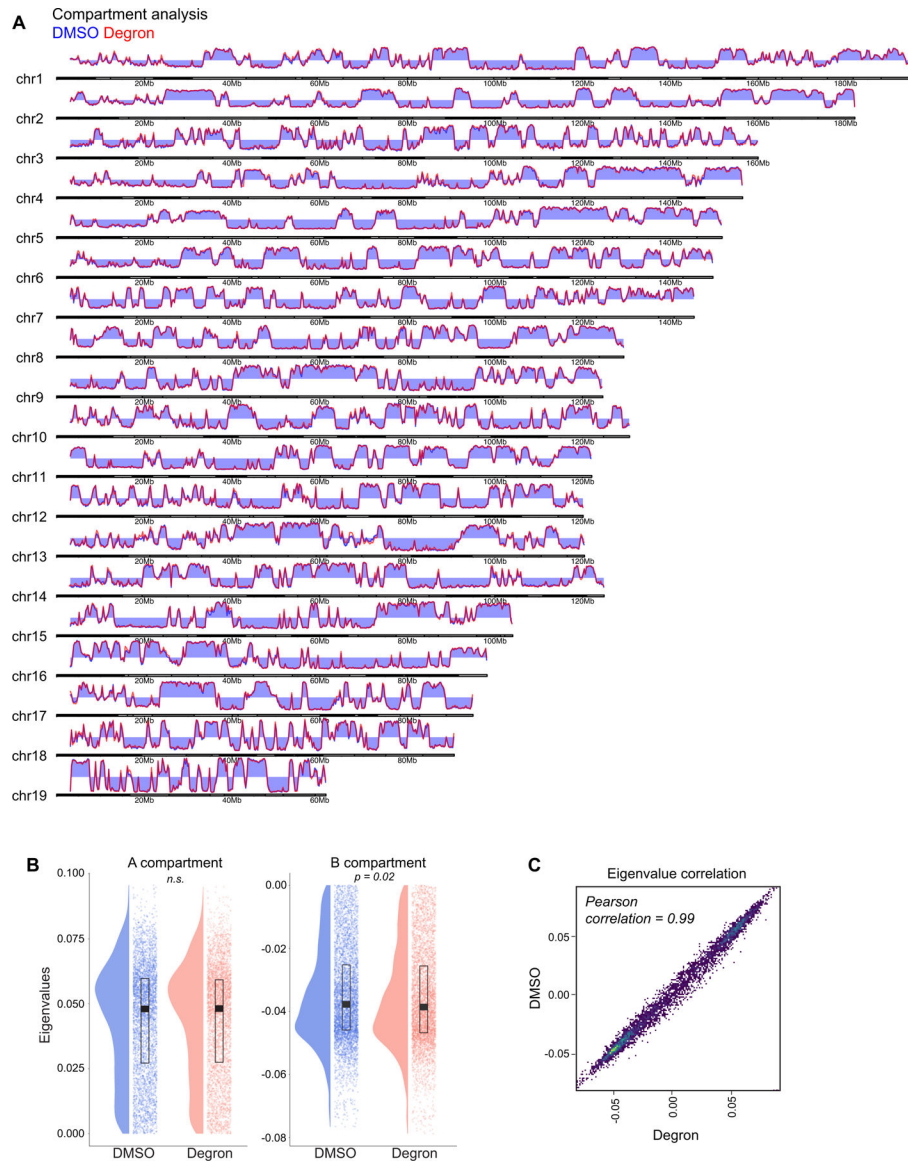
Extended Data Fig. 5. BRD4 loss does not affect compartmentalization
(A) Eigenvalues in 250 kb bins across the entire genome in DMSO (blue) and the degron (red) conditions, per chromosome. **(B)** Genome wide comparison of eigenvector values (250 kb bins) in DMSO (blue) and the degron (red) conditions. **(C)** Correlation of eigenvector values between DMSO and the degron conditions. T-test used for comparison.
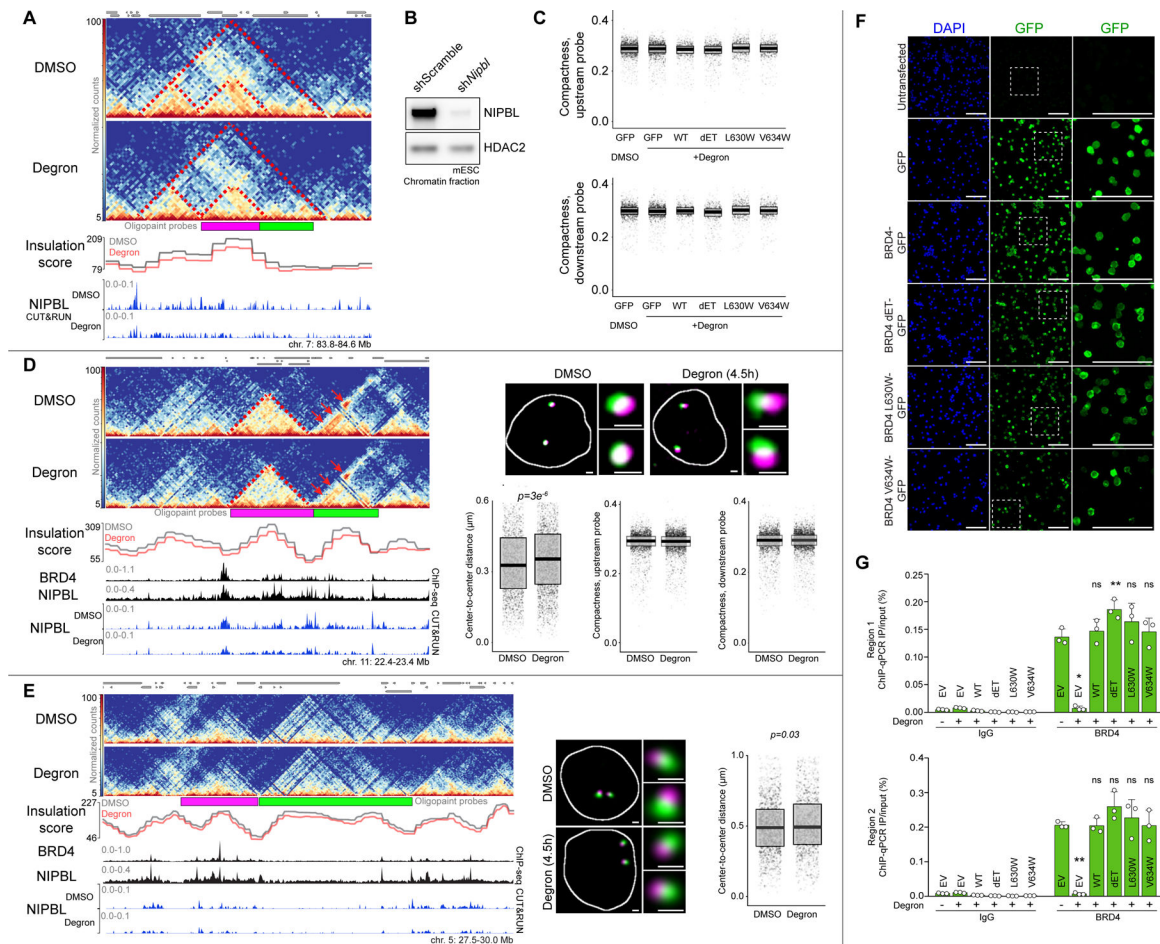
Extended Data Fig. 6. Loss of BRD4 abrogates genome folding

(A) Hi-C matrix (10 kb resolution) of region painted with Oligopaints (as indicated by the green and magenta bars below matrix, from Fig. 5a). Below matrix is insulation score and NIPBL occupancy in DMSO and degron conditions. **(B)** Immunoblot of NIPBL in shScramble and sh*Nipbl* treatment in mESCs. HDAC2 was blotted as a loading control. **(C)** FISH signal compactness (see methods) of upstream and downstream probes used in Fig. 5. **(D)** Hi-C matrix (10 kb resolution) with areas painted with Oligopaints, insulation score, BRD4 and NIPBL occupancy (in wildtype mESCs), NIPBL occupancy in DMSO and degron samples shown below. Area highlighted by red dotted line indicates subTAD and arrows point to a domain affected upon BRD4 depletion. On right is a representative image from DMSO and the degron conditions with regions painted indicated below matrix. Below the representative FISH images is the plot of center-to-center signal distances and compactness of FISH signals. For visualization purposes only, only probe center-to-center distances up to 0.6 µm shown. Wilcoxon-rank sum test. Scale bar, 1 µm. **(E)** Hi-C matrix (10 kb resolution) with areas painted with Oligopaints, insulation score, BRD4 and NIPBL occupancy (in wildtype mESCs), and NIPBL occupancy in DMSO and degron samples shown below. In middle is representative image from DMSO and the degron conditions with regions indicated on matrix painted. On right is the plot of center-to-center distances. Wilcoxon-rank sum test used for comparison. Scale bar, 1 µm. All images are maximum-

projections. **(F)** Representative GFP immunofluorescence from conditions used in Fig. 5c. Scale bar, 100 μm. **(G)** ChIP-qPCR of BRD4 or IgG at the two regions indicated in Fig. 5a by red bars. One-way ANOVA Dunnett's test was used to compare conditions to empty vector transfection with DMSO treatment. $*p<0.05$. Error bars denote the mean + SD.
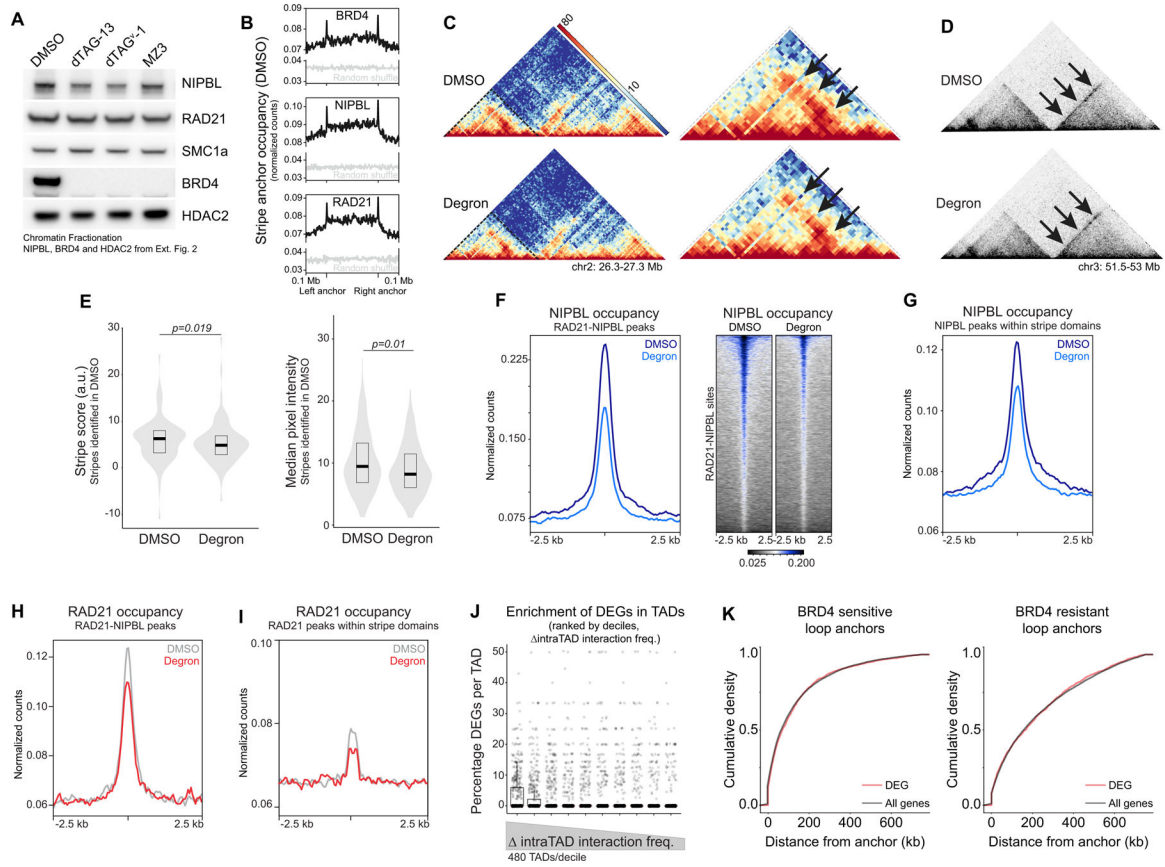
Extended Data Fig. 7. BRD4 mediates loop extrusion

(A) Chromatin fractionation immunoblot of dTAG-BRD4 mESCs treated with DMSO, dTAG-13 (500 nM), dTAG^{v}-1 (500 nM), or MZ3 (1 μM) for 4.5 hours. The NIPBL, BRD4 and HDAC2 immunoblots are reproduced from Extended Data Fig. 2f as the proteins were all blotted from the same blot. The samples were derived from the same experiment and blots were processed in parallel. **(B)** Occupancy from public datasets (see methods) of indicated factors (black) and random shuffle (gray) across stripe domains in DMSO-treated dTAG-BRD4 mESCs. Note the enrichment of factor occupancy at stripe anchors. **(C)** Hi-C matrix (top DMSO, bottom Degron) showing an example of a stripe domains (10 kb resolution), which is magnified on the right. Black arrows indicate a stripe domain which is weaker in degron compared to control. Color bar refers normalized count. **(D)** Hi-C matrix (top DMSO, bottom Degron) showing another example of stripe (indicated by arrow) which is weaker in degron compared to DMSO (10 kb resolution). **(E)** Change in stripe score and median intensity of stripe domains in degron compared to DMSO. Stripe domains defined in DMSO condition and same region compared in the degron condition. T-test used for comparison. **(F-I)** Occupancy of NIPBL (F and G) or RAD21 (H and I) at RAD21-NIPBL

peaks (F and H) or in stripe domains (G-NIPBL peaks and I-RAD21 peaks) in DMSO and the degron conditions. **(J)** The percentage of differentially expressed genes per TAD is plotted and TADs are broken into descending deciles of change in interaction frequency. Individual data points shown as well as superimposed box and whisker plot (median and interquartile range indicated by box). **(K)** Cumulative density of differentially expressed genes (DEG, FDR<0.05, |log2FC|>1, red) or all genes (black) in relation to proximity to BRD4-sensitive (left) and -resistant (right) loop anchors.
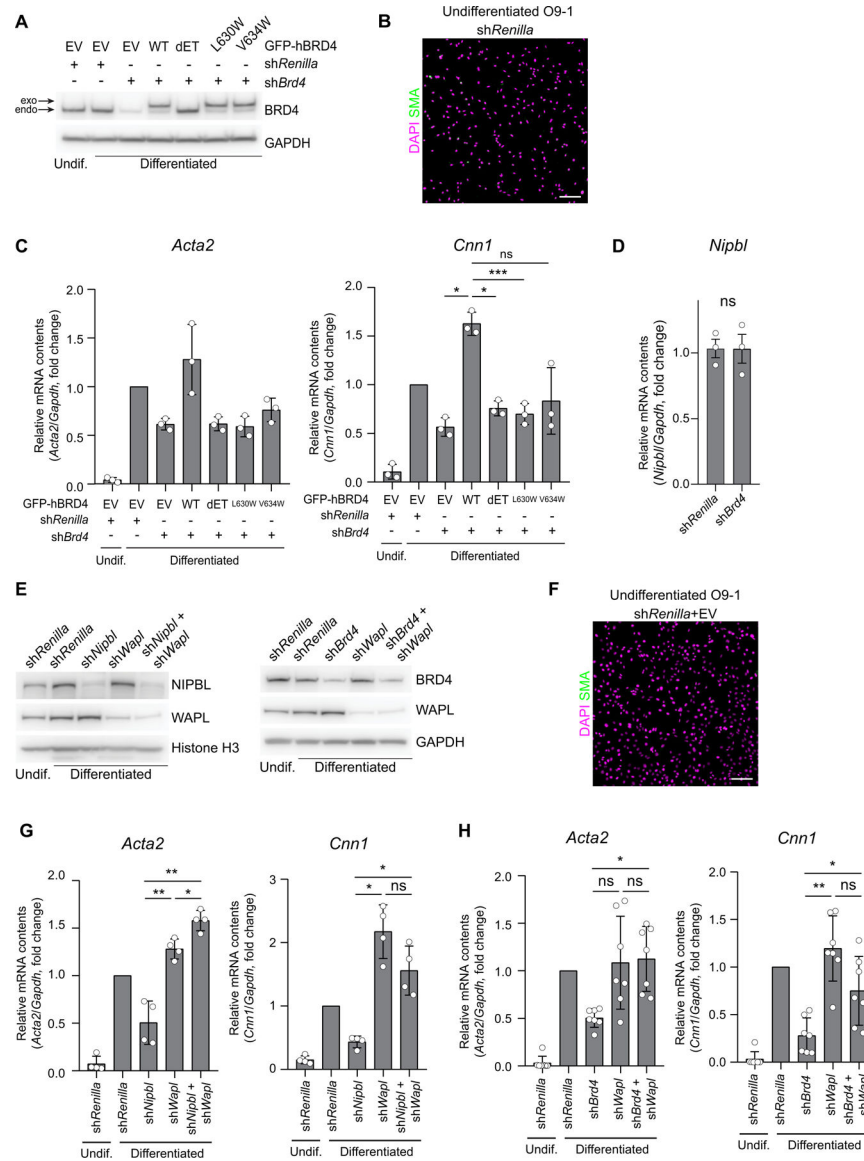
Extended Data Fig. 8. BRD4 mediates differentiation of neural crest progenitor cells
(A) Immunoblot showing levels of BRD4 upon depletion of BRD4 and introduction of wildtype BRD4 or various mutants unable to bind NIPBL. EV: empty vector. Undif.: Undifferentiated condition. **(B)** Representative image of undifferentiated O9–1 cells infected with sh*Renilla* and stained with SMA antibody. Scale bar, 100 μm. **(C)** *Acta2* and *Cnn1*

expression in indicated conditions. One-way ANOVA Tukey's multiple comparison test is used to compare across conditions (*p<0.05, ***p< 0.001). Error bars denote the mean ± SD. Undif.: Undifferentiated condition. **(D)** *Nipbl* expression in *Brd4*-depleted O9–1 cells. Unpaired t-test was used for comparison. All error bars denote the mean ± SEM. **(E)** Immunoblots of BRD4, WAPL and NIPBL in various knockdown conditions. Histone H3 and GAPDH are loading controls. Undif.: Undifferentiated condition. **(F)** Representative image of undifferentiated O91 cells infected with sh*Renilla* and transfected with empty vector and stained with SMA antibody. Scale bar, 100 μm. **(G and H)** *Acta2* and *Cnn1* expression in indicated conditions. One-way ANOVA Tukey's multiple comparison test is used to compare across conditions (*p<0.05, **p< 0.01, ***p< 0.001). Error bars denote the mean ± SD. Undif.: Undifferentiated condition.

Supplementary Material

Refer to Web version on PubMed Central for supplementary material.

Acknowledgments

References

1. Mayor R & Theveneau E. The neural crest. Development 140, 2247–2251 (2013). [PubMed: 23674598]

2. Tang W & Bronner ME Neural crest lineage analysis: from past to future trajectory. Development 147, (2020).

3. Stoller JZ & Epstein JA Cardiac neural crest. Semin Cell Dev Biol 16, 704–715 (2005). [PubMed: 16054405]

4. Vega-Lopez GA, Cerrizuela S, Tribulo C & Aybar MJ Neurocristopathies: New insights 150 years after the neural crest discovery. Developmental Biology 444, S110–S143 (2018). [PubMed: 29802835]

5. Andrey G & Mundlos S. The three-dimensional genome: regulating gene expression during pluripotency and development. Development 144, 3646–3658 (2017). [PubMed: 29042476]

6. Rowley MJ & Corces VG Organizational principles of 3D genome architecture. Nature Reviews Genetics 19, 789–800 (2018).

7. Rao SSP et al. A 3D Map of the Human Genome at Kilobase Resolution Reveals Principles of Chromatin Looping. Cell 159, 1665–1680 (2014). [PubMed: 25497547]

8. Rao SSP et al. Cohesin Loss Eliminates All Loop Domains. Cell 171, 305–320.e24 (2017). [PubMed: 28985562]

9. Wutz G et al. Topologically associating domains and chromatin loops depend on cohesin and are regulated by CTCF, WAPL, and PDS5 proteins. The EMBO Journal 36, 3573–3599 (2017). [PubMed: 29217591]

10. Kline AD et al. Diagnosis and management of Cornelia de Lange syndrome: first international consensus statement. Nature Reviews Genetics 19, 649–666 (2018).

11. Piché J, Vliet PPV, Pucéat M & Andelfinger G. The expanding phenotypes of cohesinopathies: one ring to rule them all! Cell Cycle 18, 2828–2848 (2019). [PubMed: 31516082]

12. Chatfield KC et al. Congenital heart disease in Cornelia de Lange syndrome: Phenotype and genotype analysis. American Journal of Medical Genetics Part A 158A, 2499–2505 (2012). [PubMed: 22965847]

13. Ciosk R et al. Cohesin's Binding to Chromosomes Depends on a Separate Complex Consisting of Scc2 and Scc4 Proteins. Molecular Cell 5, 243–254 (2000). [PubMed: 10882066]

14. Tonkin ET, Wang T-J, Lisgo S, Bamshad MJ & Strachan T. NIPBL, encoding a homolog of fungal Scc2-type sister chromatid cohesion proteins and fly Nipped-B, is mutated in Cornelia de Lange syndrome. Nature Genetics 36, 636–641 (2004). [PubMed: 15146185]

15. Davidson IF et al. DNA loop extrusion by human cohesin. Science (2019).

16. Kim Y, Shi Z, Zhang H, Finkelstein IJ & Yu H. Human cohesin compacts DNA by loop extrusion. Science 366, 1345–1349 (2019). [PubMed: 31780627]

17. Schwarzer W et al. Two independent modes of chromatin organization revealed by cohesin removal. Nature 551, 51–56 (2017). [PubMed: 29094699]

18. Smith TG et al. Neural crest cell-specific inactivation of Nipbl or Mau2 during mouse development results in a late onset of craniofacial defects. genesis 52, 687–694 (2014). [PubMed: 24700590]

19. Alesi V et al. Confirmation of BRD4 haploinsufficiency role in Cornelia de Lange–like phenotype and delineation of a 19p13.12p13.11 gene contiguous syndrome. Annals of Human Genetics 83, 100–109 (2019). [PubMed: 30302754]

20. Olley G et al. BRD4 interacts with NIPBL and BRD4 is mutated in a Cornelia de Lange–like syndrome. Nature Genetics 50, 329–332 (2018). [PubMed: 29379197]

21. Filippakopoulos P et al. Selective inhibition of BET bromodomains. Nature 468, 1067–1073 (2010). [PubMed: 20871596]

22. Luna-Peláez N et al. The Cornelia de Lange Syndrome-associated factor NIPBL interacts with BRD4 ET domain for transcription control of a common set of genes. Cell Death Dis 10, 548 (2019). [PubMed: 31320616]

23. Devaiah BN, Gegonne A & Singer DS Bromodomain 4: a cellular Swiss army knife. Journal of Leukocyte Biology 100, 679–686 (2016). [PubMed: 27450555]

24. Beliveau BJ et al. Versatile design and synthesis platform for visualizing genomes with Oligopaint FISH probes. PNAS 109, 21301–21306 (2012). [PubMed: 23236188]

25. Haarhuis JHI et al. The Cohesin Release Factor WAPL Restricts Chromatin Loop Extension. Cell 169, 693–707.e14 (2017). [PubMed: 28475897]

26. Tedeschi A et al. Wapl is an essential regulator of chromatin structure and chromosome segregation. Nature 501, 564–568 (2013). [PubMed: 23975099]

27. Liu NQ et al. WAPL maintains a cohesin loading cycle to preserve cell-type-specific distal gene regulation. Nature Genetics 53, 100–109 (2021). [PubMed: 33318687]

28. Kueng S et al. Wapl Controls the Dynamic Association of Cohesin with Chromatin. Cell 127, 955–967 (2006). [PubMed: 17113138]

29. Padmanabhan A et al. BRD4 (Bromodomain-Containing Protein 4) Interacts with GATA4 (GATA Binding Protein 4) to Govern Mitochondrial Homeostasis in Adult Cardiomyocytes. Circulation 142, 2338–2355 (2020). [PubMed: 33094644]

30. Lee J-E et al. Brd4 binds to active enhancers to control cell identity gene induction in adipogenesis and myogenesis. Nature Communications 8, 2217 (2017).

31. Jiang X, Rowitch DH, Soriano P, McMahon AP & Sucov HM Fate of the mammalian cardiac neural crest. Development 127, 1607–1616 (2000). [PubMed: 10725237]

32. Santos R et al. Conditional Creation and Rescue of Nipbl-Deficiency in Mice Reveals Multiple Determinants of Risk for Congenital Heart Defects. PLOS Biology 14, e2000197 (2016). [PubMed: 27606604]

33. Ishii M et al. A Stable Cranial Neural Crest Cell Line from Mouse. Stem Cells and Development 21, 3069–3080 (2012). [PubMed: 22889333]

34. Zengerle M, Chan K-H & Ciulli A. Selective Small Molecule Induced Degradation of the BET Bromodomain Protein BRD4. ACS Chem. Biol 10, 1770–1777 (2015). [PubMed: 26035625]

35. Watrin E et al. Human Scc4 Is Required for Cohesin Binding to Chromatin, Sister-Chromatid Cohesion, and Mitotic Progression. Current Biology 16, 863–874 (2006). [PubMed: 16682347]

36. Zhang Q et al. Structural Mechanism of Transcriptional Regulator NSD3 Recognition by the ET Domain of BRD4. Structure 24, 1201–1208 (2016). [PubMed: 27291650]

37. Shen C et al. NSD3-Short Is an Adaptor Protein that Couples BRD4 to the CHD8 Chromatin Remodeler. Molecular Cell 60, 847–859 (2015). [PubMed: 26626481]

38. Jung M et al. Affinity Map of Bromodomain Protein 4 (BRD4) Interactions with the Histone H4 Tail and the Small Molecule Inhibitor JQ1 *. Journal of Biological Chemistry 289, 9304–9319 (2014).

39. Crowe BL et al. Structure of the Brd4 ET domain bound to a C-terminal motif from γretroviral integrases reveals a conserved mechanism of interaction. Proc Natl Acad Sci U S A 113, 2086–2091 (2016). [PubMed: 26858406]

40. Konuma T et al. Structural Mechanism of the Oxygenase JMJD6 Recognition by the Extraterminal (ET) Domain of BRD4. Sci Rep 7, 16272 (2017). [PubMed: 29176719]

41. Hnisz D et al. Super-Enhancers in the Control of Cell Identity and Disease. Cell 155, 934–947 (2013). [PubMed: 24119843]

42. Kagey MH et al. Mediator and cohesin connect gene expression and chromatin architecture. Nature 467, 430–435 (2010). [PubMed: 20720539]

43. Nabet B et al. The dTAG system for immediate and target-specific protein degradation. Nature Chemical Biology 14, 431 (2018). [PubMed: 29581585]

44. Fernandez-Alonso R et al. Brd4-Brd2 isoform switching coordinates pluripotent exit and Smad2-dependent lineage specification. EMBO reports 18, 1108–1122 (2017). [PubMed: 28588073]

45. White J & Dalton S. Cell cycle control of embryonic stem cells. Stem Cell Rev 1, 131–138 (2005). [PubMed: 17142847]

46. Skene PJ & Henikoff S. An efficient targeted nuclease strategy for high-resolution mapping of DNA binding sites. eLife 6, e21856 (2017). [PubMed: 28079019]

47. Nabet B et al. Rapid and direct control of target protein levels with VHL-recruiting dTAG molecules. Nat Commun 11, 4687 (2020). [PubMed: 32948771]

48. Creyghton MP et al. Histone H3K27ac separates active from poised enhancers and predicts developmental state. PNAS 107, 21931–21936 (2010). [PubMed: 21106759]

49. Lieberman-Aiden E et al. Comprehensive Mapping of Long-Range Interactions Reveals Folding Principles of the Human Genome. Science 326, 289–293 (2009). [PubMed: 19815776]

50. Servant N et al. HiC-Pro: an optimized and flexible pipeline for Hi-C data processing. Genome Biology 16, 259 (2015). [PubMed: 26619908]

51. Dixon JR et al. Topological domains in mammalian genomes identified by analysis of chromatin interactions. Nature 485, 376–380 (2012). [PubMed: 22495300]

52. Nora EP et al. Spatial partitioning of the regulatory landscape of the X-inactivation centre. Nature 485, 381–385 (2012). [PubMed: 22495304]

53. Bonev B et al. Multiscale 3D Genome Rewiring during Mouse Neural Development. Cell 171, 557–572.e24 (2017). [PubMed: 29053968]

54. Cao Y et al. Accurate loop calling for 3D genomic data with cLoops. Bioinformatics 36, 666–675 (2020). [PubMed: 31504161]

55. Mumbach MR et al. HiChIP: efficient and sensitive analysis of protein-directed genome architecture. Nature Methods 13, 919–922 (2016). [PubMed: 27643841]

56. Zhang H et al. Chromatin structure dynamics during the mitosis-to-G1 phase transition. Nature 576, 158–162 (2019). [PubMed: 31776509]

57. Gong Y et al. Stratification of TAD boundaries reveals preferential insulation of super-enhancers by strong boundaries. Nature Communications 9, 542 (2018).

58. Luppino JM et al. Cohesin promotes stochastic domain intermingling to ensure proper regulation of boundary-proximal genes. Nature Genetics 52, 840–848 (2020). [PubMed: 32572210]

59. Fudenberg G et al. Formation of Chromosomal Domains by Loop Extrusion. Cell Reports 15, 2038–2049 (2016). [PubMed: 27210764]

60. Sanborn AL et al. Chromatin extrusion explains key features of loop and domain formation in wild-type and engineered genomes. Proc Natl Acad Sci U S A 112, E6456–6465 (2015). [PubMed: 26499245]

61. Vian L et al. The Energetics and Physiological Impact of Cohesin Extrusion. Cell 173, 1165–1178.e20 (2018). [PubMed: 29706548]

62. Yoon S & Vahedi G. Stripenn detects architectural stripes from chromatin conformation data using computer vision. bioRxiv 2021.04.16.440239 (2021).

63. Herzog VA et al. Thiol-linked alkylation of RNA to assess expression dynamics. Nature Methods 14, 1198–1204 (2017). [PubMed: 28945705]

64. Hug CB, Grimaldi AG, Kruse K & Vaquerizas JM Chromatin Architecture Emerges during Zygotic Genome Activation Independent of Transcription. Cell 169, 216–228.e19 (2017). [PubMed: 28388407]

65. Hsieh T-HS et al. Resolving the 3D Landscape of Transcription-Linked Mammalian Chromatin Folding. Molecular Cell 78, 539–553.e8 (2020). [PubMed: 32213323]

66. High FA & Epstein JA The multifaceted role of Notch in cardiac development and disease. Nat Rev Genet 9, 49–61 (2008). [PubMed: 18071321]

67. High FA et al. An essential role for Notch in neural crest during cardiovascular development and smooth muscle differentiation. J Clin Invest 117, 353–363 (2007). [PubMed: 17273555]

Methods References

68. Muzumdar MD, Tasic B, Miyamichi K, Li L & Luo L. A global double-fluorescent Cre reporter mouse. genesis 45, 593–605 (2007). [PubMed: 17868096]

69. Aghajanian H. et al. Pdgfrα functions in endothelial-derived cells to regulate neural crest cells and the development of the great arteries. Dis Model Mech 10, 1101–1108 (2017). [PubMed: 28714851]

70. Skene PJ, Henikoff JG & Henikoff S. Targeted *in situ* genome-wide profiling with high efficiency for low cell numbers. Nature Protocols 13, 1006–1019 (2018). [PubMed: 29651053]

71. Jones DT Protein secondary structure prediction based on position-specific scoring matrices. J Mol Biol 292, 195–202 (1999). [PubMed: 10493868]
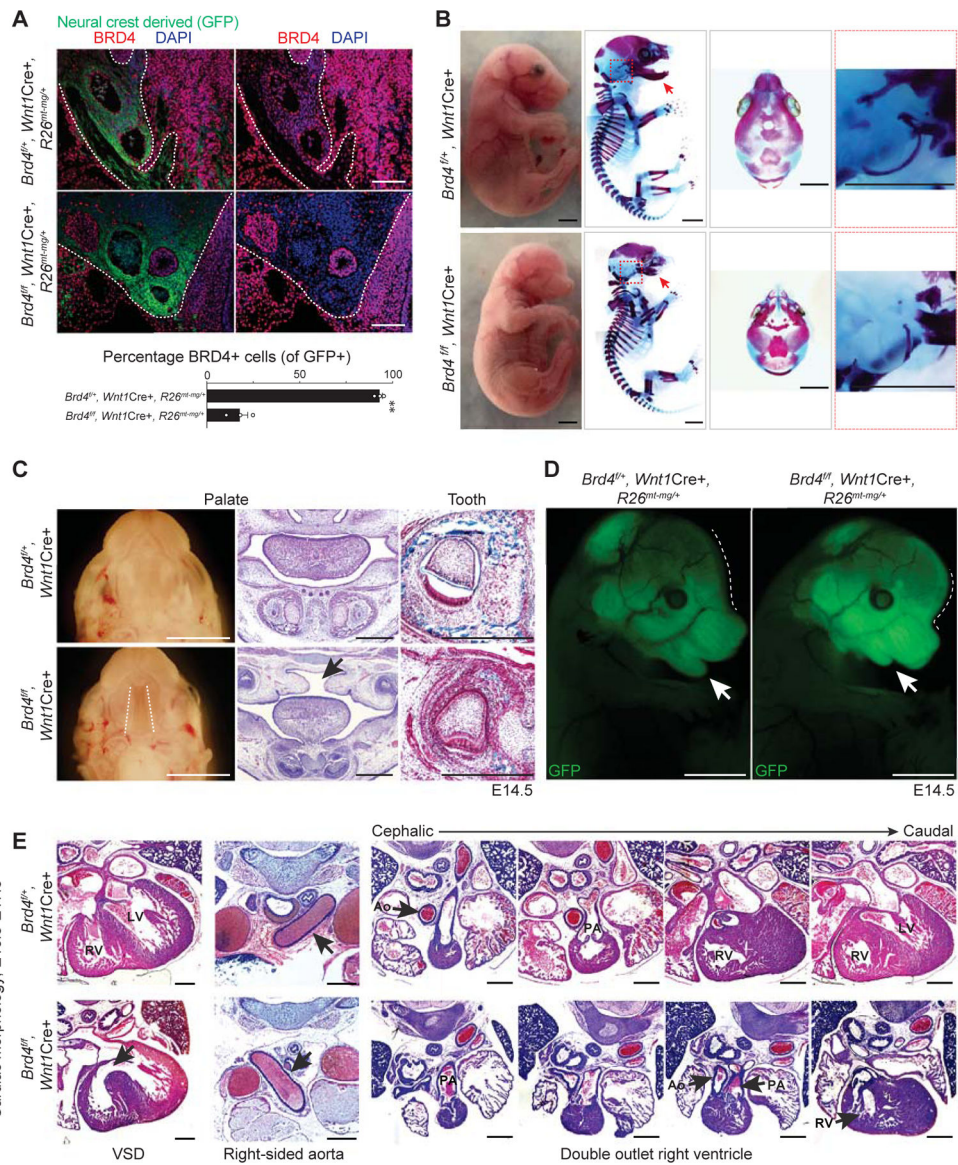
Fig. 1: Loss of Brd4 in neural crest cells results in cohesinopathy features

(A) Cross-section through aortic arch arteries of E11.5 *Brd4^f/f^, Wnt1*Cre+, *R26^mt-mg/+^* and *Brd4^f/+^, Wnt1*Cre+, *R26^mt-mg/+^* embryos stained with GFP (green, neural crest derivatives) and BRD4 (red). *t*-test, ** *P* < 0.01. Scale bars, 100 μm. All error bars denote the mean + SEM. (B) Brightfield (left) and skeletal prep images from E17.5 embryos. Sagittal view of the skeletal staining (left, composite image of multiple individual images) and axial view of the cranium (middle). Red arrow points to mandible and cochlear bones are magnified in the right panel (red box). Scale bars, 250 mm. (C) Images of the secondary palate (whole mount and histology) and teeth in E14.5 embryos. White dotted lines highlight cleft palate in mutant embryo. Adjacent to whole-mount images are H/E stained coronal sections through palate, and arrow points to cleft palate in *Brd4^f/f^, Wnt1*Cre+ embryo. On the right is a trichrome stained coronal section through developing teeth indicating reduction of collagen in *Brd4^f/f^, Wnt1*Cre+ embryo. Scale bars, 250 mm. (D) Epifluorescence images of neural

crest derivatives (GFP) in face of *Brd4^{f/f}*, *Wnt1*Cre+, *R26^{mt-mg/+}* and *Brd4^{f/+}*, *Wnt1*Cre+, *R26^{mt-mg/+}* embryos. Dotted line shows altered curvature of face in mutant embryo and arrow points to hypoplastic mandible in the mutant. Scale bars, 250 mm. **(E)** Cross-section histology of E16.5-E17.5 embryos showing examples of cardiac abnormalities in *Brd4^{f/f}*, *Wnt1*Cre+ embryos; specifically, ventricular septal defect (VSD, left), right sided aorta (R aorta, middle, arrow points to aortic arch; note aorta is coursing to the right in the mutant), double outlet right ventricle (DORV, aorta [Ao], pulmonary artery [PA], right ventricle [RV], left ventricle [LV]). Scale bars, 500 μm.
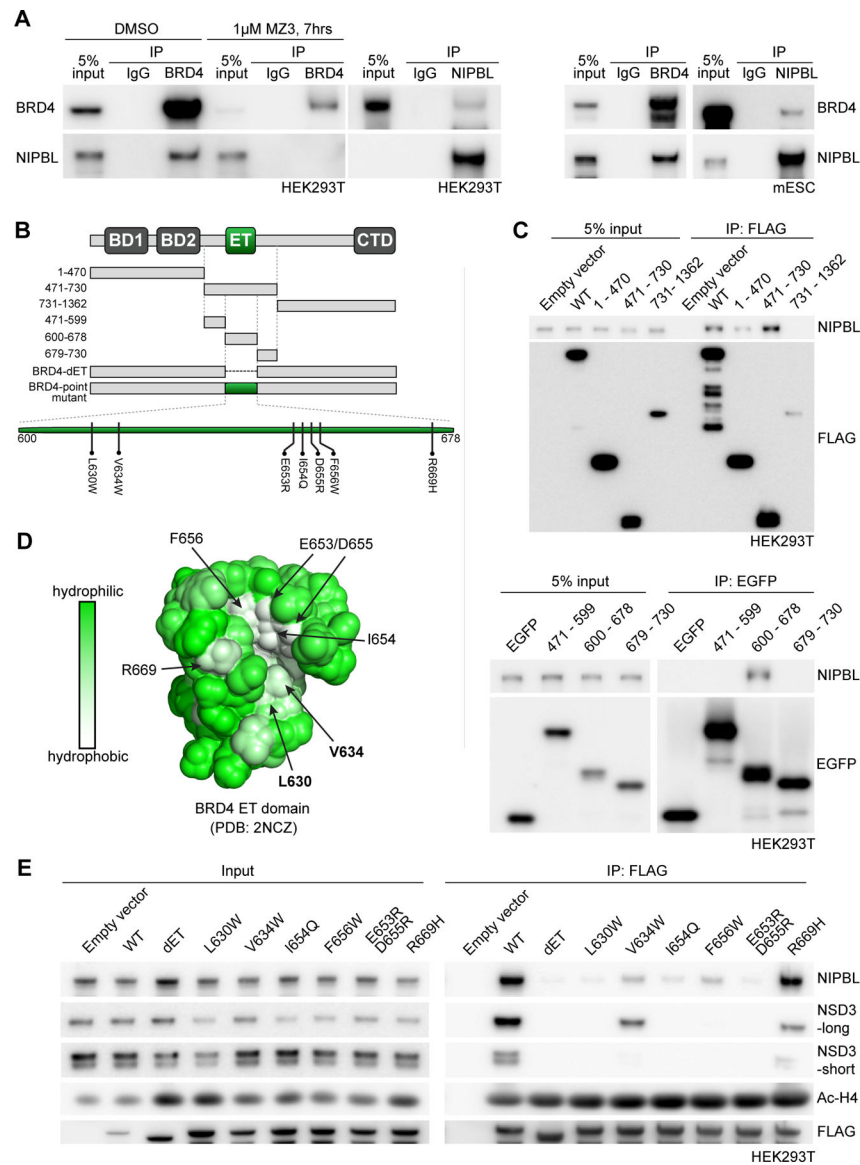
Fig. 2: BRD4 ET domain mediates a physical interaction with NIPBL

(**A**) Immunoprecipitation of endogenous BRD4 or NIPBL from HEK293T cells (left) or mESCs (right) and immunoblots probed with BRD4 or NIPBL antibody. BRD4 was immunoprecipitated in HEK293T cells treated with DMSO or 1 μM MZ3 for 7 hours. (**B**) Domain structure of BRD4 (long isoform) with schema of fragments evaluated and point mutations introduced highlighted. (**C**) FLAG- or EGFP-tagged BRD4 peptides were expressed and immunoprecipitated in HEK293T cells. Immunoblots probed with NIPBL, FLAG (top blot), and EGFP (bottom blot) antibodies. (**D**) Structure of ET domain of BRD4 highlighting the hydrophobic cleft[36]. Amino acids mutated in subsequent experiments are bolded. (**E**) Indicated FLAG-tagged versions of BRD4 were expressed and immunoprecipitated in HEK293T cells. Immunoblots probed with indicated antibodies. NSD3-long and -short indicate long and short isoforms of NSD3, respectively. Ac-H4 indicates acetylated histone H4.
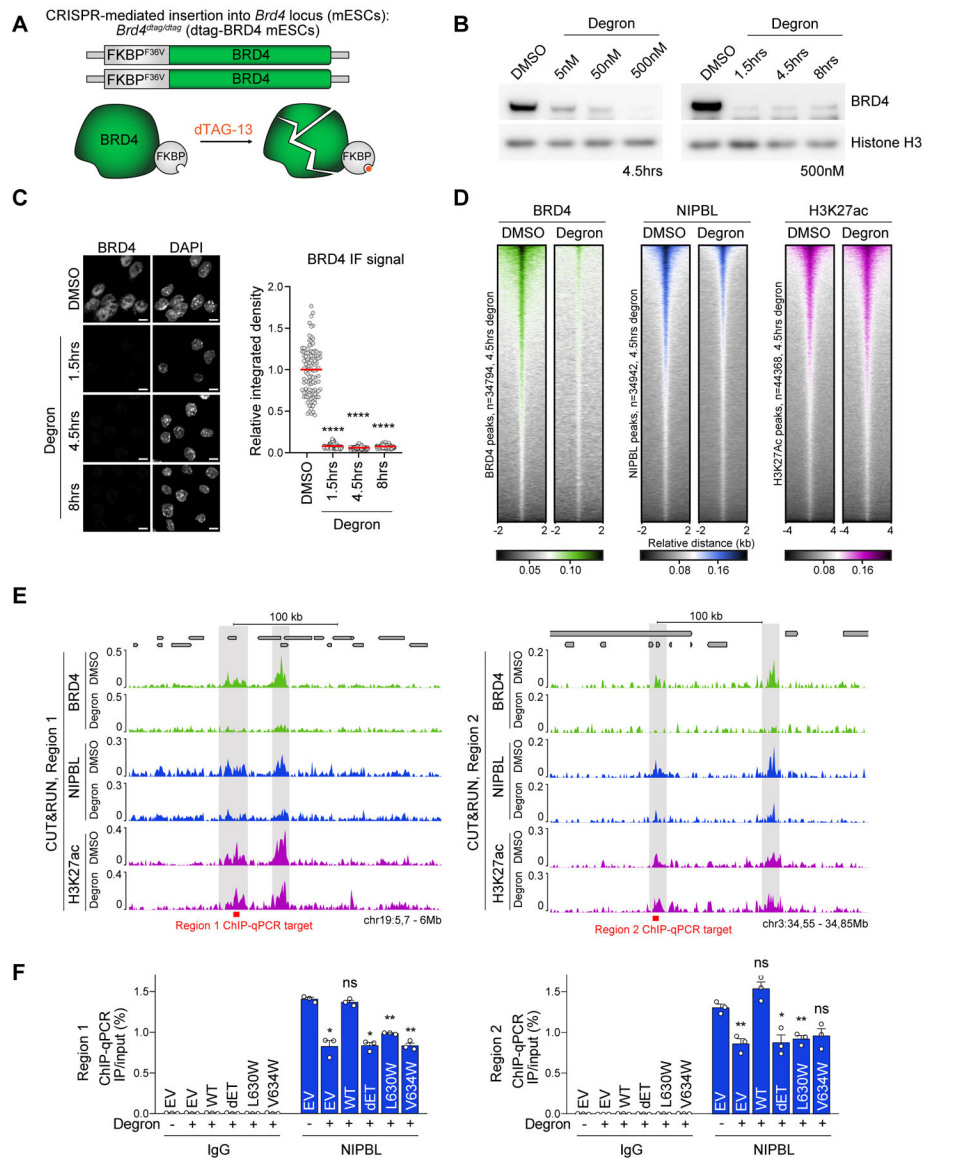
Fig. 3: Acute degradation of BRD4 reduces NIPBL occupancy on chromatin
(**A**) Schema of generating dTAG-BRD4 mESCs. (**B**) Immunoblot of BRD4 and Histone H3 on chromatin fractions from dTAG-BRD4 mESCs in various concentrations of dTAG-13 (left) or time (right). (**C**) Immunofluorescence (IF) of BRD4 and DAPI from dTAG-BRD4 mESCs treated with 500 nM dTAG-13, and associated quantification of integrated BRD4 IF signal per cell (**** P 0.0001). Mean values are indicated by red lines. Scale bar, 10 μm. (**D**) Heatmap of BRD4 (green), NIPBL (blue), and H3K27ac (purple) occupancy (normalized counts) in DMSO and the degron (4.5 hours) conditions at published peaks of each factor. (**E**) CUT&RUN tracks of BRD4 (green), NIPBL (blue) and H3K27ac (purple) in DMSO or the degron (4.5 hours) conditions at two different representative locations. ChIP-qPCR targets indicated in red. Genes shown on top of track in gray. (**F**) ChIP-qPCR of NIPBL at regions indicated in (E) in dTAG-BRD4 mESCs in DMSO or the degron conditions. Indicated full length BRD4 or BRD4-mutants which cannot bind NIPBL were

simultaneously expressed. EV: empty vector. One-way ANOVA Dunnett's test was used to compare conditions to empty vector transfection with DMSO treatment. * $P < 0.05$, ** $P < 0.01$. Error bars denote the mean + SEM.
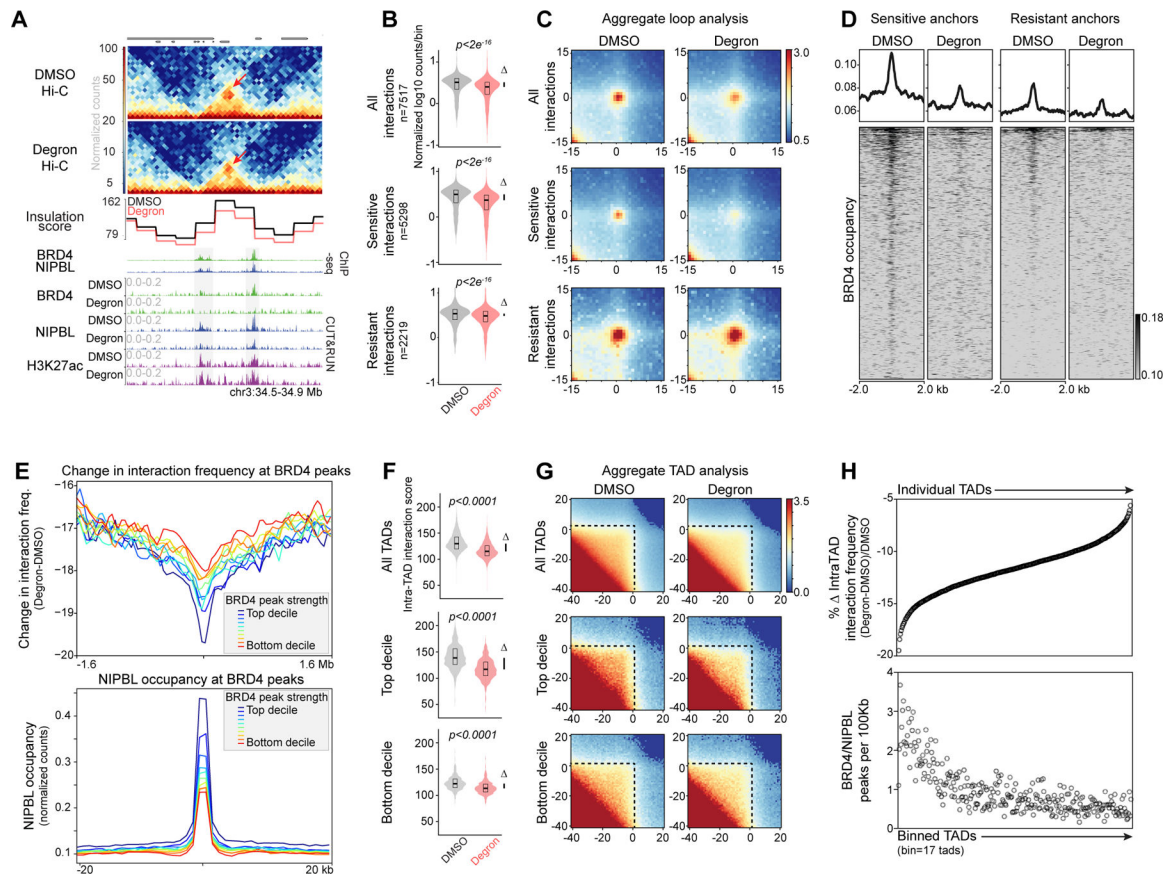
Fig. 4: BRD4 maintains genome folding

(**A**) Insulation score and representative Hi-C matrix view (10-kb resolution) in DMSO and the degron (4.5 hours) conditions with occupancy of BRD4 (green), NIPBL (blue), and H3K27ac (purple) below. Occupancy from publicly available BRD4 and NIPBL ChIP-seq datasets in mESCs is also shown. Genes are shown above Hi-C matrix in gray. Red arrow points to corner peak which is weaker in the degron condition. (**B and C**) Violin plots (B) of mean counts/bin in indicated subsets of chromatin loops and associated aggregate plot analysis (C). *t*-test was used for comparison. (**D**) BRD4 occupancy (normalized counts) at anchors of BRD4-sensitive and -resistant interactions in the DMSO or the degron conditions. Note the enrichment of BRD4 at the anchors of BRD4-sensitive loops. (**E**) Change in interaction frequency at BRD4 peaks (stratified into deciles of peak strength) upon depletion of BRD4 (top). NIPBL occupancy (normalized counts) at stratified BRD4 peaks in DMSO condition (bottom). (**F and G**) Violin plots of interaction frequency (F) and associated aggregate plots (G) of different subsets of TADs in DMSO and the degron conditions. Two-tailed *t*-test was used for comparison in (F). Color bars in (C) and (G) refer to enrichment score. (**H**) Percentage change in intra-TAD interaction frequency upon BRD4 loss of regions defined as TADs in DMSO condition (ranked in descending change in frequency order, top). Number of BRD4/NIPBL peaks (per 100 kb) per 17 consecutive TADs shown below (ordered based on descending change in interaction frequency). Bar under Δ in (B) and (F) indicates median-to-median difference. All boxes in violin plots indicate median and interquartile range.
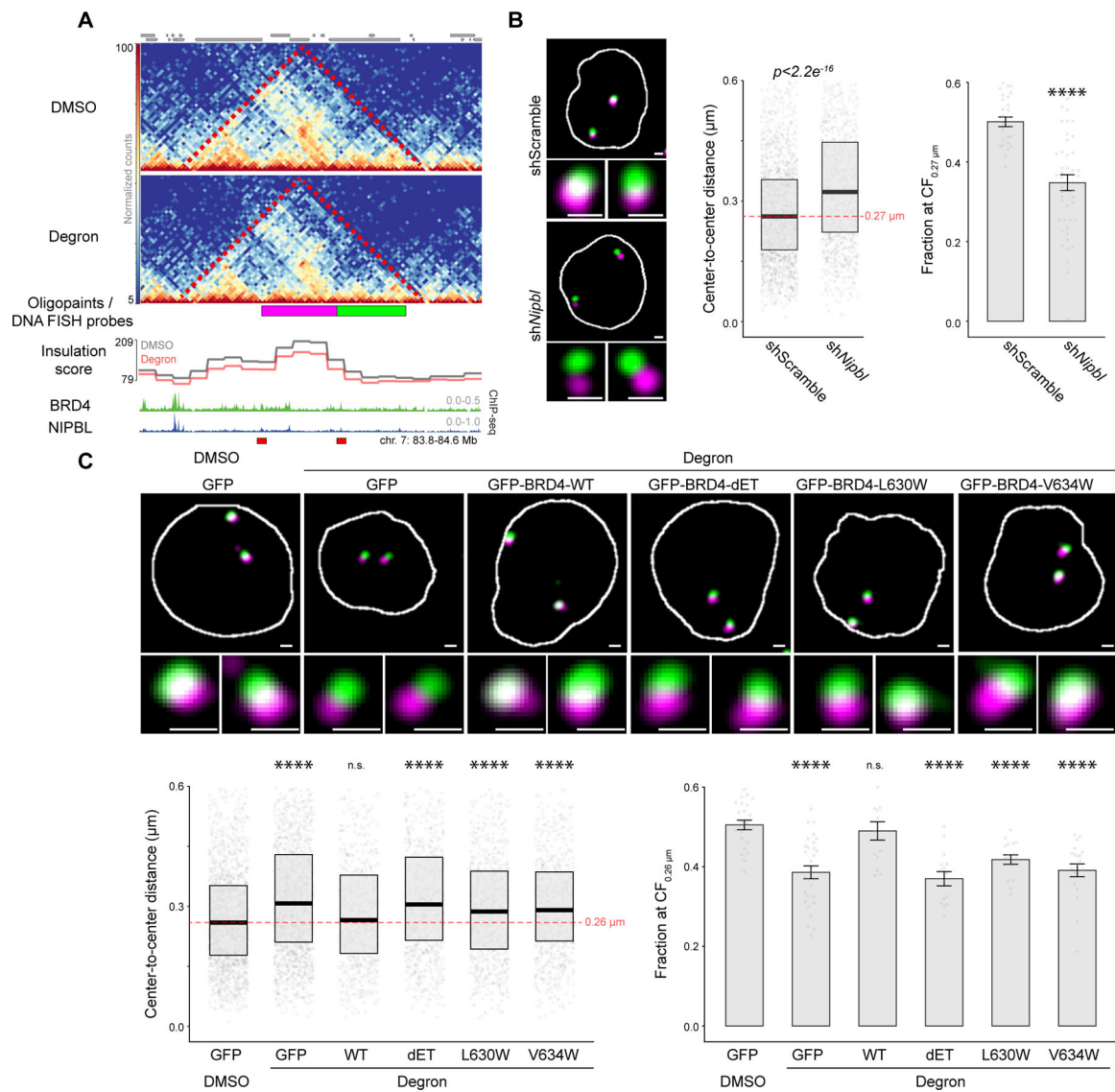
Fig. 5: A BRD4-NIPBL interaction is necessary for genome organization

(A) Hi-C matrix (10-kb resolution) of genomic region painted with Oligopaints (as indicated by the green and magenta bars below the matrix). Below matrix is insulation score and occupancy of BRD4 and NIPBL (ChIP-seq) in mESCs. Two red bars below matrix indicate the targets for ChIP-qPCR (Extended Data Fig. 6g). Regions 1 and 2 in Extended Data Figure 6g are indicated by left and right bars, respectively. **(B)** Representative images of DNA FISH to regions indicated in (A) in dTAG-BRD4 mESCs expressed with shScramble or sh*Nipbl*. Adjacent to images are plots of center-to-center distance (n > 1,000 each condition, welch two sample *t*-test) and fraction of signals in each field of view below median contact frequency (0.27 μm, red dotted line) of center-to-center distance in shScramble condition (**** *P* < 0.0001, Wilcoxon-rank sum test). **(C)** Representative Images of DNA FISH of regions indicated in (A) in dTAG-BRD4 mESCs treated with DMSO or dTAG-13 for 4.5 hours. Cells were also transfected with plasmids encoding indicated BRD4 fragment (or GFP control). Below high-magnification images is the

quantification of center-to-center distance (n > 700 each condition, all comparisons to GFP/DMSO, **** $P < 0.0001$, Wilcoxon-rank sum test) and fraction of signals in each field of view at median contact frequency of center-to-center distance in GFP/DMSO conditions (all comparisons to GFP/DMSO, **** $P < 0.0001$, Wilcoxon-rank sum test). CF denotes contact frequency at 0.26 μm (red dotted line). For visualization purposes only, only probe center-to-center distances up to 0.6 μm shown in (B) and (C) barplots. Scale bars, 1 μm. All error bars denote the mean ± SEM; all boxes indicate median and interquartile range. All images are maximum intensity-projected. Nucleus boundary is marked by white line.
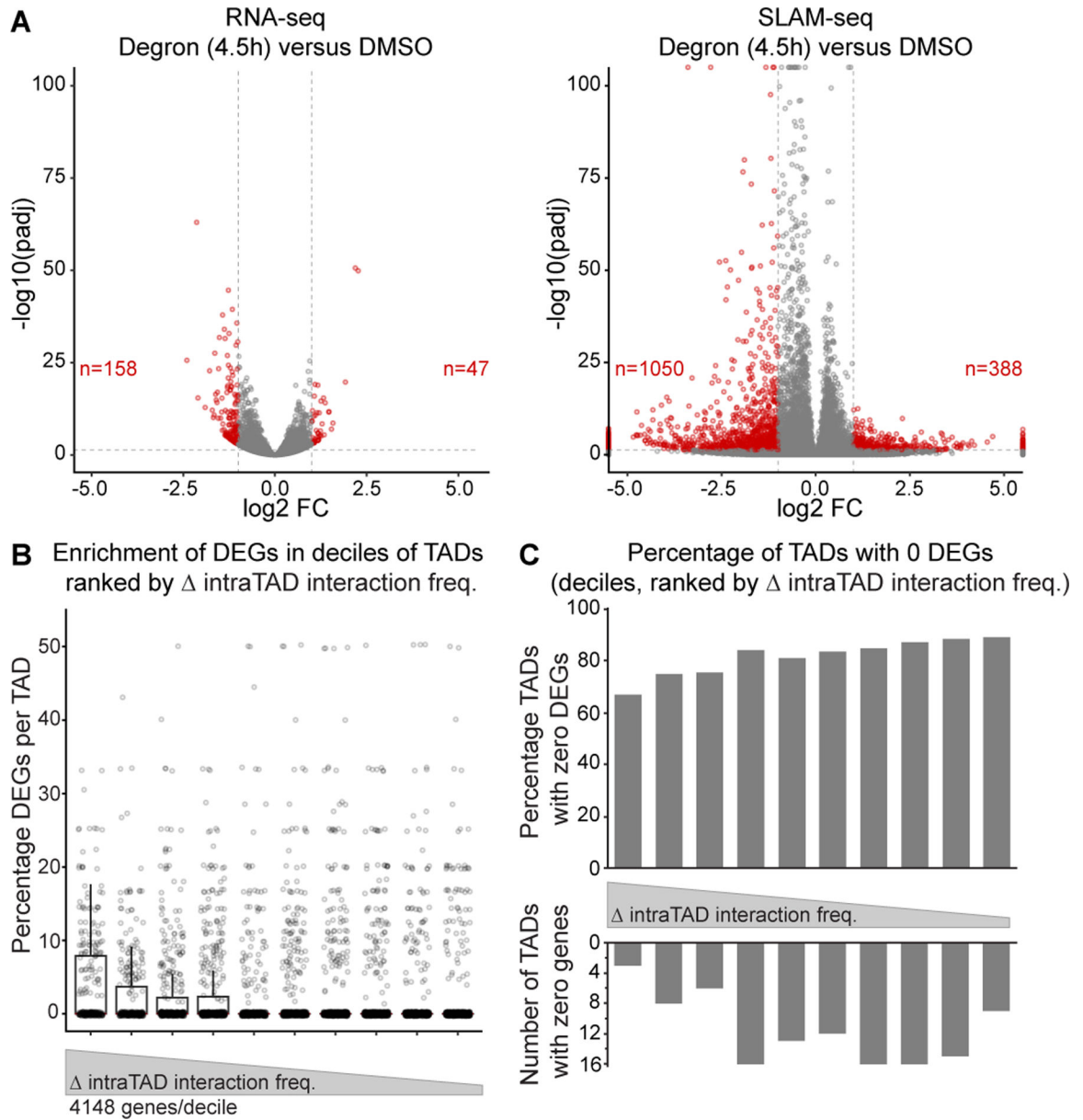
Fig. 6: Changes in transcription dynamics upon BRD4 depletion
(A) Volcano plots plotting change in gene expression in the degron (4.5 hours) versus DMSO conditions. On left is RNA-seq while right shows increased sensitivity of SLAM-seq. Dotted lines indicate thresholds used to defined differential expression (FDR > 0.05, $|\log_2 \text{FC}| > 1$). Number of upregulated or downregulated genes indicated on plots. **(B)** The percentage of differentially expressed genes per TAD is plotted and TADs are broken into descending deciles of change in interaction frequency. Individual TADs shown as well as superimposed box and whisker plot (median and interquartile range indicated by box). Only TADs with at least 1 gene plotted. **(C)** Percentage of TADs at each decile with zero DEGs (top) and number of TADs with zero genes (bottom).
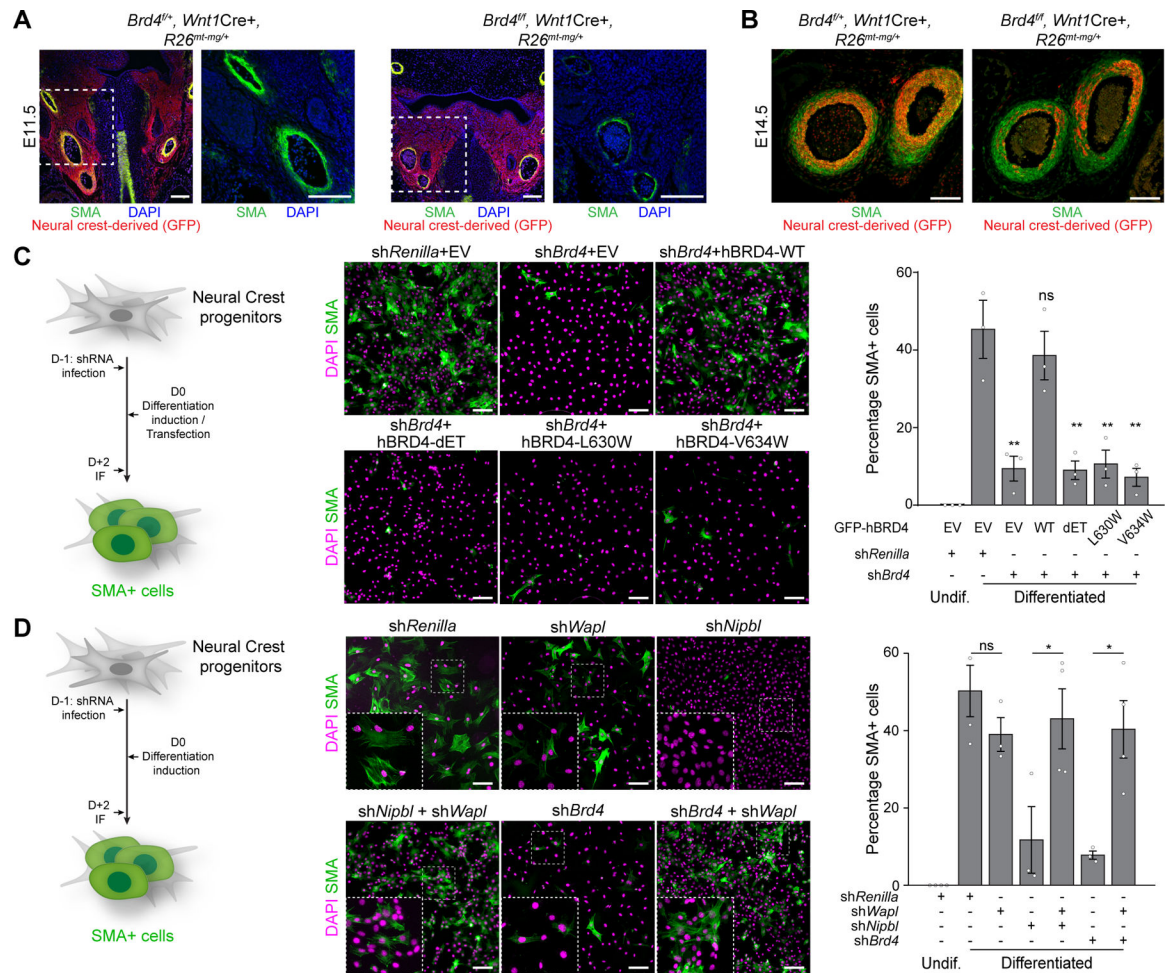
Fig. 7: A BRD4-NIPBL interaction promotes smooth muscle cell differentiation of neural crest cells

(A and B) Coronal section of E11.5 (A) and E14.5 (B) *Brd4^{f/f}, Wnt1*Cre+, *R26^{mt-mg/+}* and *Brd4^{f/+}, Wnt1*Cre+, *R26^{mt-mg/+}* aortic arch arteries stained with GFP (red, neural crest derivatives) and smooth muscle actin (SMA, green), area in box magnified in middle panel of (A). Scale bar, 100 μm. **(C)** Differentiation of neural crest progenitor cells (O9–1 cells) upon knockdown of endogenous *Brd4* and exogenous expression of indicated human BRD4 mutants unable to bind NIPBL. Schema on left, representative images of SMA (green) and DAPI (magenta) in middle, quantification of replicate experiments tallied on right. EV: empty vector. ** $P < 0.01$, ANOVA followed by Dunnett's test. Scale bar, 100 μm. All error bars denote the mean ± SEM. **(D)** Differentiation of neural crest progenitor cells (O9–1 cells) upon knockdown of indicated factors, individually or in combination. Schema on left, representative images of SMA (green) and DAPI (magenta) in middle, insets display higher magnification images of the outlined area, quantification of replicate experiments tallied on right. * $P < 0.05$, ANOVA followed by Tukey's test. Scale bar, 100 μm. All error bars denote the mean ± SEM.
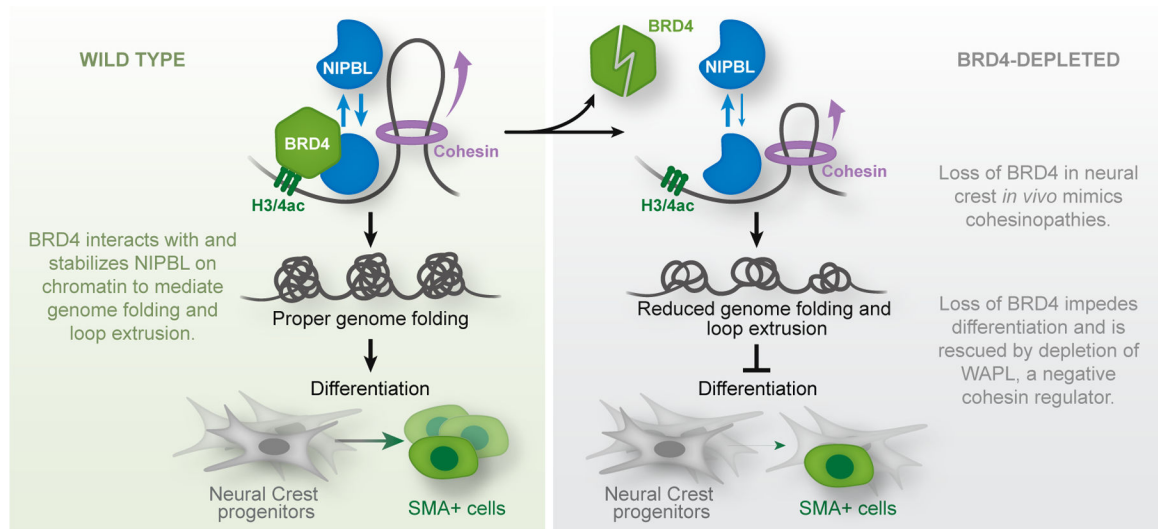
Fig. 8: Model depicting proposed mechanism of action of BRD4 to stabilize NIPBL on chromatin to maintain chromatin interactions and loop extrusion.

Loss of BRD4 reduces NIPBL occupancy and leads to loss of genome folding and neural crest differentiation. Restoration of the mechanisms underlying genome folding restores neural crest progenitor differentiation.